ANALYSIS AND MODELING OF CAPACITIVE MEMS GYROSCOPES WITH

FEEDBACK CONTROL

By

WEI CUI

A thesis submitted in partial fulfillment of
the requirements for the degree of

MASTER OF SCIENCE IN MECHANICAL ENGINEERING

WASHINGTON STATE UNIVERSITY VANCOUVER
School of Engineering and Computer Science

August 2010

To the Faculty of Washington State University:

       The members of the Committee appointed to examine the thesis of   WEI CUI find it satisfactory and recommend that it be accepted.

<div style="text-align:right">

_____

Xiaolin Chen, Ph.D., Chair

_____

Wei Xue, Ph.D., Chair

_____

Hakan Gurocak, Ph.D.

</div>

ACKNOWLEDGMENT

I am deeply grateful to Professor Xiaolin Chen and Professor Wei Xue for introducing me the amazing world behind MEMS. I would like to thank them for their continuous guidance and support, and for providing the ideal environment to do the research. I must thank Professor Hakan Gurocak for invaluable discussions and advice. Thank you for sharing your expertise with me.

I also really appreciate my lab-mates David Binion, Menglu Wu, Pengfei Li and Niel Hayes for the technical discussions and the friendly lab environment.

Lastly, I would like to express my warmest gratitude to my parents, the Straub family, and my friends for their love and always support.

ANALYSIS AND MODELING OF CAPACITIVE MEMS GYROSCOPES

WITH FEEDBACK CONTROL

Abstract

by Wei Cui, M.S.
Washington State University
August 2010

Chair: Xiaolin Chen and Wei Xue

The fast development of MEMS gyroscopes requires the mass production of devices with high performance, high robustness, and low cost. MEMS devices have been traditionally analyzed using finite element method (FEM) and boundary element method (BEM). However, these methods have tradeoffs in time, skill level restrictions, and limitations on the scope of the design problem. One goal of this thesis is to investigate MEMS gyroscopes using system-level models which significantly accelerate the design process and improve the device performance. The 3D gyroscope models are generated based on mask layout and fabrication process restrictions. This practice reduces the number of prototyping cycles needed to complete the product design.

Micro-fabrication imperfections and environmental variations lead to significant uncertainties of the performance of MEMS devices in mass production. This thesis also investigates compensator designs of resonant and non-resonant MEMS gyroscopes to provide robustness against structural and environmental parameter variations. The compensators are designed via the Linear Quadratic Regulator (LQR) technique in MATLAB. The closed-loop MEMS device performance is simulated using system-level models in CoventorWare. Simulation shows that the closed-loop gyroscope achieves high

linearity, wide dynamic range, and high robustness. Our results demonstrate that LQR is an effective design to control MEMS gyroscopes and provides high robustness against fabrication imperfections.

TABLE OF CONTENTS

LIST OF TABLES

LIST OF FIGURES

CHAPTER ONE

INTRODUCTION

1.1 Overview

Microelectromechanical systems (MEMS) represent the technology that integrates electrical and mechanical systems at the micro level. Developed from the semiconductor fabrication technologies, the most promising feature of the MEMS technology is its capability of building very sophisticated systems on silicon substrates [1].

New MEMS devices are developed and reported every year. Many of these devices are commercially successful such as ink-jet nozzles, pressure sensors, accelerometers, and micro-mirrors. More types of MEMS devices have been developed lately, including microfluidic devices, gyroscopes, micro phones, and radio frequency (RF) MEMS. Potential MEMS market is estimated to be $17 billion by 2015 [2].

MEMS inertial sensors, consisting of accelerometers and gyroscopes, are an important group of MEMS devices [3]. They are among the most commercialized devices with the market size of approximately $2 billion in 2009 and have a wide range of applications in automotive industry, consumer electronics, defense & aerospace field, and industrial & medical field [4]. MEMS accelerometers have the second largest MEMS market after pressure sensors. It is believed that MEMS gyroscopes will soon become mass produced at similar volumes. In 2009, millions of units of MEMS gyroscopes were produced worldwide, corresponding to a $750 million market [4]. Due to the complex motion, MEMS gyroscopes have not been able to attract a lot of attention until recent years. Unlike accelerometers, which detect the linear motion, gyroscopes measure the

angular velocity of the system in the inertial reference frame. By integrating the measured angular velocity with the known initial conditions, the orientation of the system can be obtained and updated in real time [5].

1.2 MEMS gyroscopes

The fundamental operation principle of MEMS gyroscopes is based on the Coriolis force effect. In physics, the motion of an object in an inertial frame of reference is governed by Newton's laws. The Coriolis force effect appears when transforming Newton's laws from an inertial frame of reference to a rotating frame of reference. The resulting Coriolis acceleration is proportional to the cross product of the angular rate and the velocity of the object. The direction is orthogonal to the direction of the rotation and the velocity of the object.

Although various designs of MEMS gyroscopes, such as oscillating beams [6, 7], vibrating rings [8] and tuning forks [9, 10], have been developed, unlike macro-scale gyroscopes which have rotating parts, the majority of MEMS gyroscopes use vibrating mechanical elements. Because no rotating part is involved, vibratory gyroscopes are subject to less friction and wear. In a fixed frame of reference, the vibrating element, or so called the proof mass of a MEMS gyroscope is actuated into the drive mode oscillation. When the frame of reference begins to rotate, the proof mass is then subject to a Coriolis force. The Coriolis force effect causes an energy transfer process from the drive mode oscillation into the sense mode oscillation that can be measured.

The actuation mechanisms which are used to drive the proof mass could be electrostatic [8, 9, 11], electromagnetic [10, 12], or piezoelectric [6, 7, 13-16].

Electrostatic actuation is based on the electrostatic force generated between electrically charged particles. Electromagnetic actuation relies on the electromagnetic force which is the product of current across a conductor moving through a magnetic field. Piezoelectric actuation depends on piezoelectric effect, an ability of some materials to generate mechanical stress in response of electric field or potential. The sense mechanisms can be piezoelectric [13-16], capacitive [6-12], or piezoresistive [20, 21]. Because the piezoelectric effect is reversible, piezoelectric effect can be used to detect angular rate induced stress in the sense mode of MEMS gyroscopes. Parallel plate structure is a common design of capacitive detection. The gap change between the plates due to the sense mode motion can be converted to the capacitance change. The piezoresistive effect is a property of some materials that cause a change in resistance due to applied mechanical stress. Piezoresistive devices are easy to fabricate and require low output impendence compared to capacitive devices, while they are vulnerable to temperature variations.

Depending on the material of the structure, MEMS gyroscopes can be roughly divided into silicon gyroscopes and non-silicon gyroscopes. The common fabrication processes for the silicon MEMS gyroscopes include: bulk micromachining and wafer bonding [8, 9, 11, 20], surface micromachining [17-19], and combined bulk-and-surface micromachining [12, 21]. Bulk micromachining traditionally implies the use of subtractive processes and produces structures inside a substrate. In most bulk micromachining processes, two or more silicon wafers are bonded, and the structures are made out of the whole thickness of a silicon wafer. In contrast to subtractive bulk micromachining, surface micromachining uses successive deposition and etching of thin

3

structural layers on top of a substrate. Combined bulk-and-surface micromachining take the advantages of both surface and bulk micromachining.

Based on their performance, MEMS gyroscopes belong to one of the classes: Rate grade, Tactical grade, and Inertial grade devices. The requirements for the three classes are listed in Table 1.1 [5]. Primarily, MEMS gyroscopes used in automotive applications require Rate grade performance. Truly low-cost and high-performance MEMS gyroscopes are not on the market yet. Relatively high prices of the currently available devices limit their uses to the customer applications. Moreover, lower grade performance restricts their applications in many areas. Therefore, pressure on developing high performance, high robustness, and low cost devices is enormous.

Table 1.1. Performance requirements for three classes of gyroscopes [5].

Parameter	Rate grade	Tactical grade	Inertial grade
Resolution, °/h/√Hz	>30	3-30	<0.06
Bias drift, °/h	10-1000	0.1-10	<0.01
Scale factor accuracy, %	0.1-1	0.01-0.1	<0.01
Full scale range, °/s	50-1000	>500	>400
Maximum shock in 1 ms, g	10^3	10^3-10^4	10^3
Bandwidth, Hz	>70	≈100	≈100

1.3 Review of MEMS gyroscopes developments

In early 1980's, piezoelectric quartz vibratory gyroscopes were successfully demonstrated. Some commercialized examples included fused-quartz Hemispherical Resonator Gyro by Delco [13], quartz angular rate sensor by BEI Systron Donner

Automotive Division [14], and quartz rate gyro sensor by Toyota [15]. In 1995, Bosch introduced electronic stability program (ESP) system for the Mercedes-Benz S-Class sedan, assisting drivers to keep their vehicles on track in critical driving circumstances [16]. The first ESP system used a quartz gyroscope which was piezoelectrically actuated. Although quartz gyroscopes could achieve very high quality factors at atmospheric pressure with high performance, the fabrication processing was not compatible with integrated circuit (IC) fabrication technology.

The Draper Laboratory demonstrated the first silicon-based MEMS resonant gyroscope in 1991 with a resolution of $4°/s/\sqrt{Hz}$ [11]. The gyroscope was a bulk micromachined device; it was driven by the electrostatic force. The maximum sensitivity was obtained when the sense mode is driven at the resonant frequency of the drive mode. The fabrication process for the silicon was easily integrated with signal readout, signal processing, and control electronics. Therefore, after successful demonstration of the silicon gyroscope, some efforts were initiated to substitute quartz gyroscopes with silicon MEMS gyroscopes. Later in 1993, The Draper Laboratory reported their next generation silicon-on-insulator (SOI) tuning-fork gyroscopes which were fabricated through bulk micromachining and wafer bonding [9]. The proof mass was electrostatically vibrated in the in-plane drive mode using four set of comb drives (Figure 1.1). The maximum displacement of the proof mass could reach 10 μm.
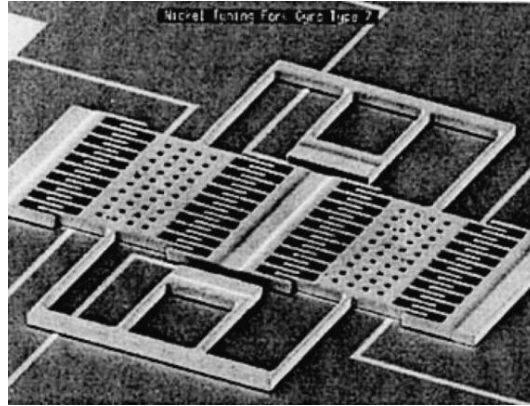
Figure 1.1. Scanning electron microscopy (SEM) image of the prototype tuning-fork

gyroscope from the Draper Laboratory [9].

In 1994, researchers at General Motors and the University of Michigan developed a vibrating ring gyroscope [8]. The sense mode was capacitively monitored. Because of its symmetric structure, it was less sensitive to temperature drift. The frequency mismatch due to the fabrication uncertainties can be electronically compensated. The device demonstrated a resolution of 0.5 °/s in a 25 Hz bandwidth. The operation temperature range was from -40 to 85 °C. The scale factor accuracy was less than 3% over the whole temperature range.
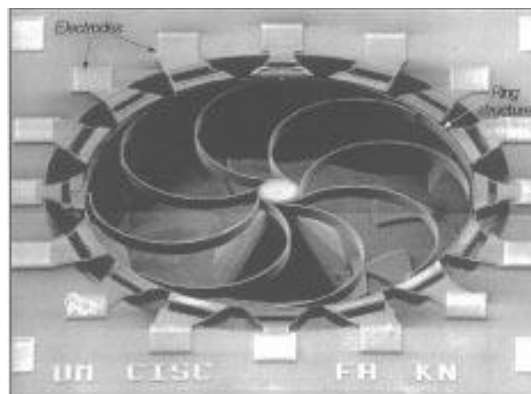
Figure 1.2. SEM image of the ring gyroscope from the University of Michigan [5].

The first silicon gyroscope used in ESP systems, DRS-MM1, was introduced by Bosch in 1998. The reported electromagnetically excited tuning-fork gyroscope was able to achieve large actuation range as large as 50 μm at 2 kHz [12]. The resulting Coriolis acceleration was 220 mg at 100 °/s rotation and the sensitivity was 18 mV/(°/s). The temperature drift was less than 0.5 °/s. A permanent magnet was mounted inside the package. The device was fabricated through a combination of bulk and surface micromachining processes. Although large actuation amplitude could increase the sensor sensitivity, it led to the fatigue problem over the long haul. The second generation gyroscope, DRS-MM2, was introduced in 2001 [17]. It was a circular-shape device with four sets of curved comb fingers (Figure 1.3). This device was fabricated with surface micromachining. It achieved a measuring range of ±100 °/s and a resolution of 0.04 °/s/√Hz. The third generation gyroscope, DRS-MM3, also targeting ESP systems was reported in 2005 [18]. Through vacuum packaging, the device achieved a bias instability of 1.35 °/h and a resolution of 8.82 °/h/√Hz at 60 Hz bandwidth, showing its potential for Tactical grade performance. The operation temperature range was from -40 to 120 °C. The temperature drift over the whole temperature range was less than ±0.4 °/s. However, the scale factor of ±2.5% and the measuring range of ±187 °/s still stayed in Rate grade class.
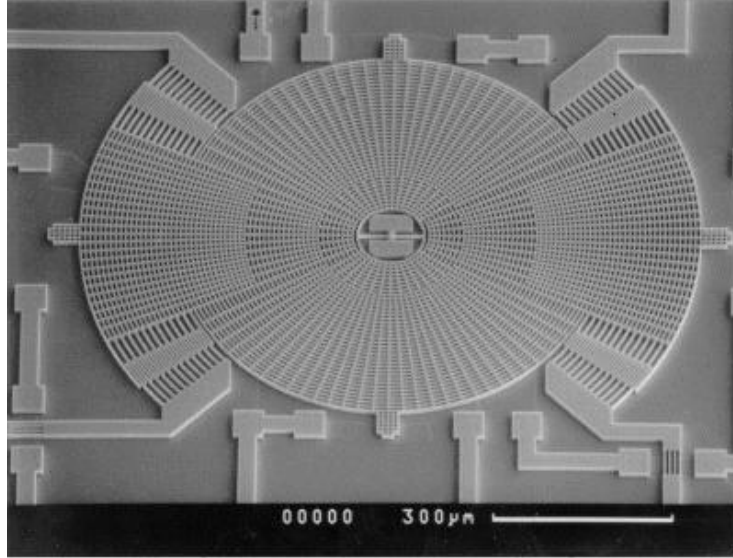
Figure 1.3. SEM image of the circular shape gyroscope four sets of curved comb fingers from Bosch [17].

Traditionally, the proof mass of the MEMS gyroscope is driven into resonance in the drive-mode direction by an external actuation force. When the gyroscope is subject to an angular rotation, a Coriolis force generated in the sense-mode direction is proportional to the angular rate input. Ideally, the resonance of the drive and the sense modes is designed to maximize the response gain and the sensor sensitivity. Therefore, the sense and the drive modes should have the same resonant frequency. The output signal is amplified by the quality factor Q of the sense mode, resulting in the maximum gain output.

The quality factor Q is a dimensionless parameter that describes how damped an oscillator is. To achieve a high Q, internally less-damped material such as quartz can be used. Q also rises rapidly under low viscous damping which can be obtained with vacuum packaging. However, high Q comes with many disadvantages for the mode-matching gyroscopes which involve extreme control of device fabrication process. Given

that a sense mode system has a resonant frequency of 10 kHz with a 5 Hz mismatch between the drive mode frequency and sense mode frequency, the output gain drops 29% under a Q of 1000 but 90% under a Q of 10000 [1]. The sensitivity of the resonant gyroscope deteriorates significantly with the high Q. With a 10 Hz mismatch, the output gain drops 55% under a Q of 1000 and 95% under a Q of 10000 [1]. This means for an additional 5 Hz mismatch, the output gains drops another 26% under a Q of 1000 and 5% under a Q of 10000. Therefore, the sense mode frequency is commonly designed to be slightly off the drive mode frequency to improve the robustness, while intentionally sacrificing sensor output and sensitivity.

Because of this tradeoff, non-resonant gyroscope designs which use dynamic amplification instead of resonance are developed [22-28]. The devices are inherently robust against the resonant frequency shift due to the fabrication uncertainties and environmental parameter variations. The important development milestones are investigated as follows.

In 2001, Cenk Acar and Andrei M. Shkel at the Microsystems lab at the University of California, Irvine proposed the first non-resonant gyroscope idea which was a four degrees-of-freedom (4-DOF) with a 2-DOF drive mode oscillator and a 2-DOF sense mode oscillator (Figure 1.4). The new paradigm in MEMS gyroscope provided inherent robustness against structural and environmental parameter variations [22]. A 0.05 μm deviation from 2 μm nominal beam width or a 0.1 μm deviation from 2 μm nominal structure thickness resulted in less than 1% in the gain. The device was fabricated with surface micromachining. The proof mass was electrostatically driven in-

9

plane using two sets of comb drives. The deflection of the sense mode motion was detected through the parallel plate capacitors connected to the moving proof mass.
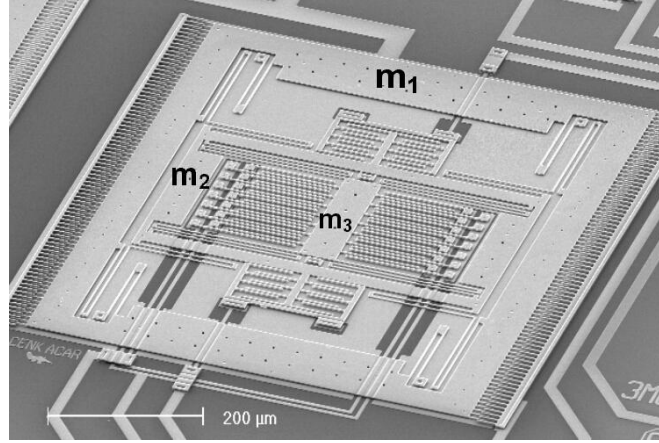
Figure 1.4. SEM image of a surface-micromachined 4-DOF non-resonant gyroscope from the Microsystems Laboratory at the University of California, Irvine [23].

Later in 2003, Cenk Acar and Andrei M. Shkel reported a torsional surface micromachined 3-DOF non-resonant gyroscope with a 2-DOF drive mode oscillator and one single DOF sense mode oscillator [24]. A torsional 2-DOF oscillator was formed by an active gimbal and a passive gimbal in the drive-mode direction. The excitation force was applied on the active gimbal. The frequency response of the drive mode had two resonance peaks and a flat region between the peaks, where the amplitude was less sensitive to parameter variations. A 1-DOF torsional oscillator in the sense-mode direction operated at the resonance; its resonant frequency was designed to coincide with the flat region of the drive mode as shown in Figure 1.5. Therefore, the design eliminated the mode-matching requirement by using dynamic amplification instead of resonance in the drive-mode direction. Large amplitude of the sense mode oscillation was achieved with small actuation amplitude. The design was expected to overcome the small

electrostatic actuation range while achieve improved robustness against fabrication imperfections.
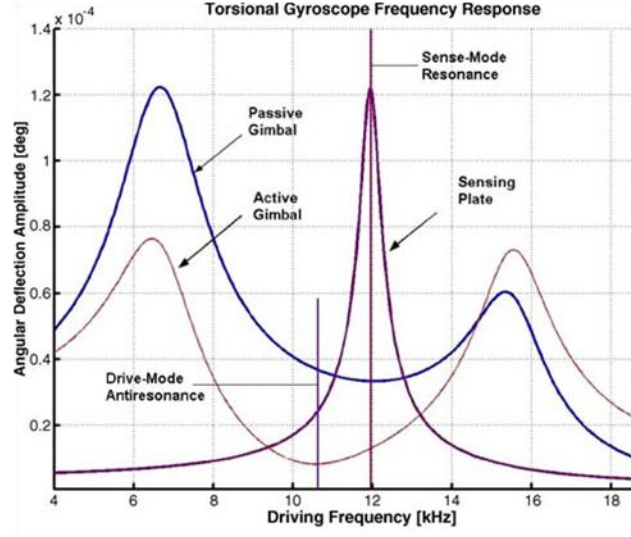
Figure 1.5. The frequency responses of the 2-DOF drive and 1-DOF sense modes [24].

In 2005, a distributed-mass gyroscope with eight DOFs in the drive mode was proposed in order to achieve large bandwidth as well as high gain output [25]. This device was fabricated with bulk micromachining and wafer bonding. The structure was shown in Figure 1.6. The eight drive mode resonant frequencies were actively tuned to be incrementally spaced. The resulting total frequency response of the drive mode achieved a wide bandwidth with the leveled amplitude (Figure 1.7). Although a wide open-loop bandwidth (a few hundred Hz) was achieved at atmospheric pressure, a maximum gain variation of 17.2 % was observed due to the fabrication imperfections.

11
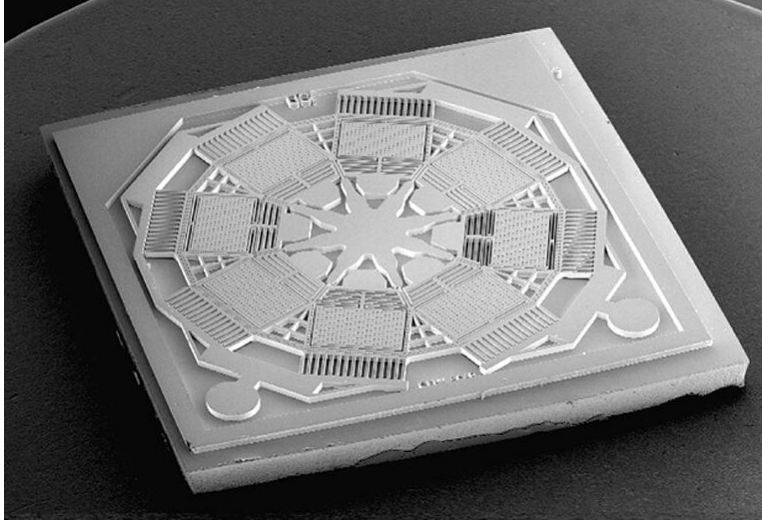
Figure 1.6. SEM of a distributed-mass non-resonant gyroscope [25].

(a)

(b)
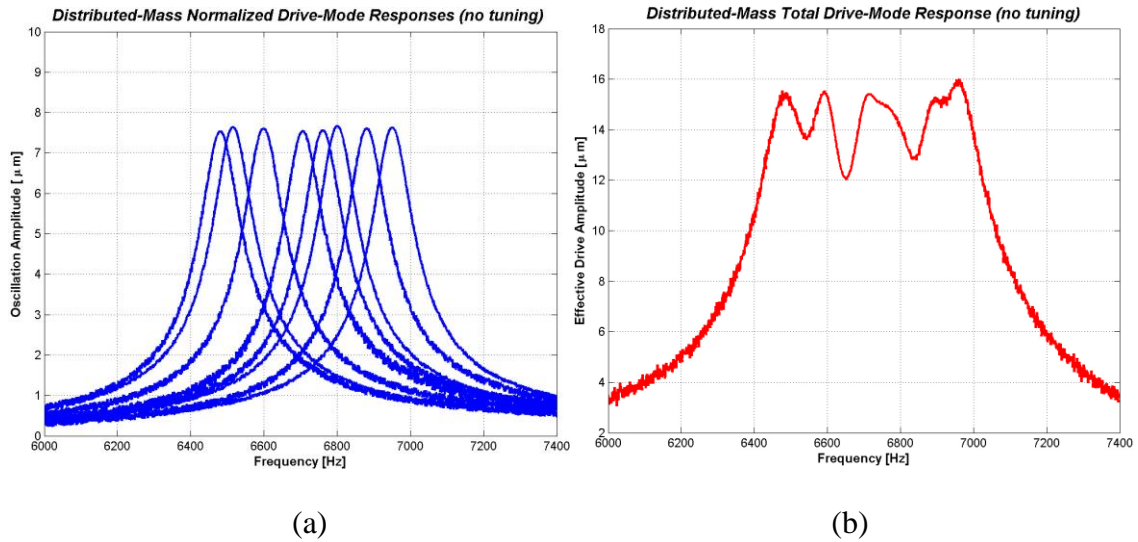
Figure 1.7. (a) The frequency responses of the drive mode oscillators and (b)

experimental frequency response of the total dirve-mode response [25].

In 2006, BEI Systron Donner Automotive Division and the University of California, Irvine reported a linear bulk micromachined 3-DOF non-resonant gyroscope with one single DOF drive mode and a 2-DOF sense mode [26]. The prototype gyroscope achieved a resolution of 0.64 °/s/√Hz at 50 Hz bandwidth in atmospheric pressure.

12

In 2008, Alexander Trusov et al. improved the 3-DOF design [27, 28]. The prototypes were characterized in air and demonstrated the resolution and bias drift of 0.09 °/s/√Hz and 0.08 °/s, respectively. The non-resonant gyroscope had low noise levels even without costly vacuum packaging. The uncompensated temperature coefficients of bias and scale factor were 313 °/h/°C and 351 ppm/°C. Although the non-resonant gyroscope designs still stay on the research stage and the performance is generally worse than some high-performance resonant gyroscopes, its performance has been improved since its first prototype came out in 2001. Furthermore, the inherently robust structure provides the device with very low noise level in air.

In summary, since the first silicon MEMS gyroscope reported almost two decades ago, the resolution and the bias drift have been continuously improved, showing the potential Tactical grade performance. However, the scale factor accuracy and the temperature drift still remain at two to three orders of magnitude lower level, staying in the Rate grade category. There are a few factors from several different domains contribute to the challenges in MEMS gyroscopes. First, the coupling domains of MEMS gyroscopes hamper the fast development of new designs. MEMS devices have traditionally simulated using FEM and BEM analysis; however, these methods have tradeoffs in time, skill level requirements, and limitations on the scope of the design problem. Second, tolerances of micro-fabrication process lead to significant uncertainties of device performance in mass production. Despite the remarkable improvement in the device performance, measurement repeatability is not concluded to be promising for commercialization. Third, the variations of package condition, such as temperature and pressure inside the package, give rise to performance drifts in the sensor scale factor and

temperature coefficient. To achieve reliable performance, many available gyroscopes on the market are costly vacuum packaged which cost 80% of the total cost [29].

1.4 Scope of the thesis

The fast development of MEMS gyroscopes requires the mass production of devices with high performance, low cost, ease of fabrication, efficient packaging, and the ability to integrate the devices with control circuits. Typical MEMS simulation mainly focuses on device performance without considering fabrication capabilities and packaging integratibility. One important goal of this thesis is to realize fast simulation in CoventorWare to enable the rapid design of MEMS gyroscopes involving interactions between different physical domains with the objective of shortening development time and reducing costs. Ideally, all the aspects of MEMS design need to be carefully considered ranging from material selection, structure layout, fabrication capabilities, to packaging integratibility. To keep up with the design complexity, MEMS researchers are relying more on MEMS simulation tools so that the device performance can be verified and optimized prior to any prototyping or system integration. Nevertheless, typical MEMS simulation that involves both structural (full model) and circuitry (reduced order model) modeling are often performed using general-purpose tools that traditionally exist in two different engineering fields. Design communication is hard to achieve with these discipline-specific packages. Modeling results from different physical domains as well as results at different levels of abstraction cannot be easily related or integrated.

From the development of the MEMS gyroscopes, despite continuously improvement of the resolution and the bias drift, the scale factor accuracy still stays at the

Rate grade performance. The other goal of this research is to design robust controllers for MEMS gyroscopes to improve the scale factor accuracy under the fabrication uncertainties. Proportional-integral-derivative (PID) feedback mechanism is the most widely used in industrial control systems. With the PID controllers, the design system can be easily implemented but the trial-and-error process does not guarantee control optimality. In this research, we investigate a compensator design in state space using the optimal LQR. LQR technique provides optimal closed-loop poles which achieve varying balances between a fast system response and a low control effort. The optimum performance of the controller is obtained with less iterations of trial and error.

1.5 Structure of the thesis

In this chapter, an overview of MEMS gyroscopes is presented.

In Chapter 2, the structure and basic dynamics of resonant and non-resonant gyroscopes are described. The LQR state-space feedback control techniques are introduced.

In Chapter 3, the simulation that incorporates process modeling, device analysis, device optimization, and package analysis is performed for a resonant gyroscope.

In Chapter 4, the compensator is developed for a resonant gyroscope. The closed-loop gyroscope aims to achieve high linearity, wide dynamic range, and high robustness to fabrication imperfections.

In Chapter 5, the simulation that incorporates device analysis and optimization is performed for a non-resonant gyroscope. The viscous damping is solved in the FEM

solver and the results are imported into system-level simulation to accurately estimate damping effect on the model.

In Chapter 6, the compensator using LQR is developed for a non-resonant gyroscope. The closed-loop non-resonant gyroscope is expected to have better system response and scale factor accuracy.

In Chapter 7, a summary of the contributions of this research is given and the future research directions are discussed.

CHAPTER TWO

BASIC PRINCIPLES OF CAPACITIVE MEMS GYROSCOPES

2.1 Resonant gyroscopes

The first silicon MEMS gyroscope developed in 1991 is a resonant gyroscope. The resonant gyroscope combines a proof mass and suspension beams to form a 1-DOF oscillator in both the drive and sense-mode directions as shown in Figure 2.1.
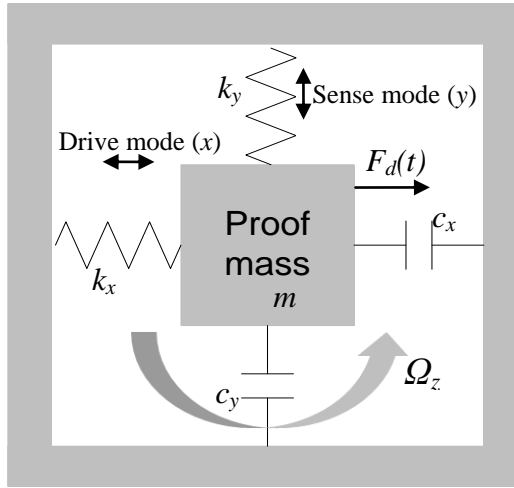
Figure 2.1. Schematic of a vibratory gyroscope. The proof mass is free to oscillate in the drive and sense-mode directions.

In the drive-mode direction, the proof mass is driven into resonance by a sinusoidal electrostatic force $F_d(t)$ at the drive mode resonant frequency. The proof mass vibrates along the drive-mode direction (x). Once the device is subject to the angular velocity Ω_z, Coriolis force effect appears and drives the proof mass into oscillation in the sense-mode direction (y).

2.1.1 Dynamic system modeling

Based on Figure 2.1, the overall dynamics of the gyroscope can modeled by the mass-damper-spring system and simplified as:

$$m\ddot{x} + c_x\dot{x} + k_x x = F_d(t) \tag{2.1}$$

$$m\ddot{y} + c_y\dot{y} + k_y y = 2m\Omega_z\dot{x} \tag{2.2}$$

where m, c, and k are proof mass, damping coefficient, and spring constant, respectively. The subscript x and y denote the direction. Eqn. (2.1) is the system equation for the drive mode. Eqn. (2.2) is the system equation for the sense mode. The term $2m\Omega_z\dot{x}$ in the sense mode equation is the rotation-induced Coriolis force. After taking Laplace transform, Eqn. (2.1) and Eqn. (2.2) and become:

$$X(s) = \frac{F_d(s)}{ms^2 + c_x s + k_x} \tag{2.3}$$

$$Y(s) = \frac{2m\Omega_z X(s)s}{ms^2 + c_y s + k_y} \tag{2.4}$$

where $s = j\omega$ is the Laplace variable, $F_d(t) = F_0 sin(\omega t)$. The amplitude $x(t)$ and amplitude $y(t)$ under the excitation force can be obtained as:

$$x(t) = \frac{F_0}{m\sqrt{\left(\omega_d^2 - \omega^2\right)^2 + \left(2\zeta\omega_d\omega\right)^2}} \sin(\omega t + \varphi_d) \tag{2.5}$$

$$y(t) = \frac{2\Omega_z\omega F_0}{m\sqrt{\left(\omega_d^2 - \omega^2\right)^2 + \left(2\zeta_d\omega_d\omega\right)^2}} \frac{1}{\sqrt{\left(\omega_s^2 - \omega^2\right)^2 + \left(2\zeta_s\omega_s\omega\right)^2}} \sin(\omega t + \varphi_s) \tag{2.6}$$

where $\omega_d = \sqrt{\dfrac{k_x}{m}}$ and $\omega_s = \sqrt{\dfrac{k_y}{m}}$ are the resonant frequencies of the drive and sense modes, respectively. $\zeta_d = \dfrac{c_x}{2\sqrt{mk_x}}$ and $\zeta_s = \dfrac{c_y}{2\sqrt{mk_y}}$. φ_d and φ_s are the phases of drive

and sense modes, respectively. From Eqn. (2.6), when $\omega_d = \omega_s$, $y(t)$ achieves the maximum value.

2.2 Non-resonant gyroscopes

All the non-resonant gyroscope designs reported so far offer improved robustness by increasing the DOF of the dynamical system. Dynamic systems with more coupled proof masses have more resonance peaks. In this research, we investigate a 4-DOF non-resonant gyroscope with a 2-DOF drive mode oscillator and a 2-DOF sense mode oscillator. The same as a resonant gyroscope, the non-resonant gyroscope can be lumped into the oscillator models in the drive mode and the sense-mode directions (Figure 2.2). In each direction, the oscillator has two DOFs which induce two resonance peaks.

(a)   (b)
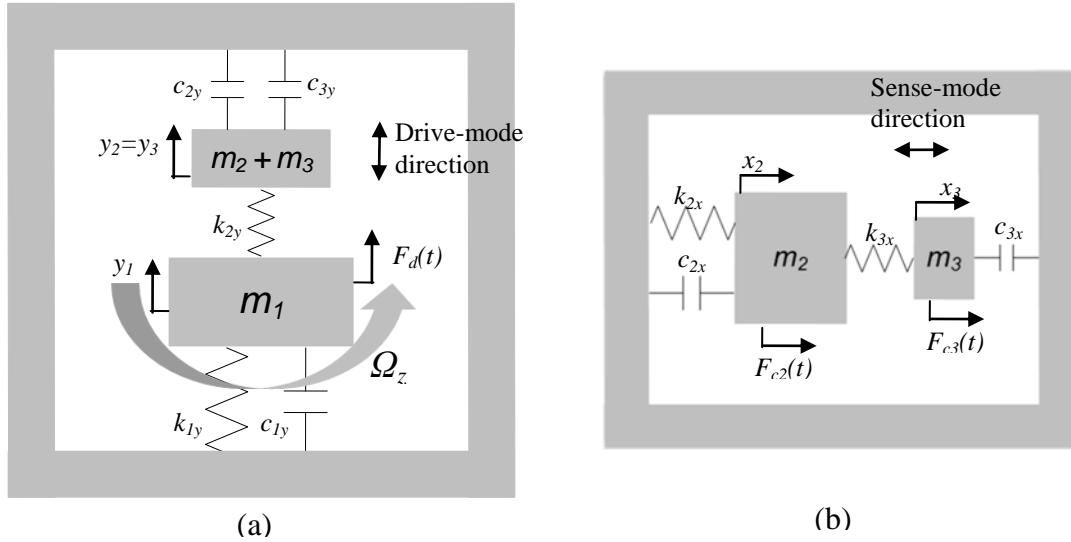
Figure 2.2. Lumped models of the 4-DOF non-resonant gyroscope: (a) 2-DOF drive mode (y_1 and y_2) and (b) 2-DOF sense mode (x_2 and x_3).

m, c and k stand for proof mass, damping coefficient, and spring constant, respectively. Subscript x and y indicate the direction. Subscript 1, 2, and 3 indicate the relevance with

proof masses m_1, m_2, and m_3, respectively. $F_d(t)$ is sinusoidal excitation force. $F_{c2}(t) = 2m_2\Omega_z\dot{y}_2$ and $F_{c3}(t) = 2m_3\Omega_z\dot{y}_2$ are rotation-induced Coriolis forces. m_1 of the 2-DOF drive mode oscillator is driven into resonance by $F_d(t)$. m_1 and the combination of m_2 and m_3 form a 2-DOF drive oscillator. m_2 and m_3 are free to move independently in the sense-mode direction and form a 2-DOF sense oscillator. The excitation force $F_{c2}(t)$ and $F_{c3}(t)$ are applied on m_2 and m_3, respectively.

2.2.1 Dynamic system modeling

Based on Figure 2.2, the system governing equations of the drive mode motion can be given by:

$$m_1\ddot{y}_1 + c_{1y}\dot{y}_1 + k_{1y}y_1 = k_{2y}(y_2 - y_1) + F_d(t) \tag{2.7}$$

$$(m_2 + m_3)\ddot{y}_2 + c_{2y}\dot{y}_2 + k_{2y}y_2 = k_{2y}y_1 \tag{2.8}$$

Eqn. (2.7) is the system equation for the proof mass m_1. Eqn. (2.8) is the system equation for the combination of m_2 and m_3. The excitation force $F_d(t)$ is applied on m_1. Therefore, m_1 is the active mass and the combination of m_2 and m_3 is the passive mass.

Take the Laplace transform of the system equations of the drive mode motion of Eqn. (2.7) and Eqn. (2.8):

$$Y_1(s) = \frac{\left((m_2 + m_3)s^2 + c_{2y}s + k_{2y}\right)F_d(s)}{m_1(m_2 + m_3)s^4 + \left(c_{1y}(m_2 + m_3) + c_{2y}m_1\right)s^3 + \left(c_{1y}c_{2y} + m_1k_{2y} + (k_{1y} + k_{2y})(m_2 + m_3)\right)s^2}$$
$$\overline{+\left(k_{1y}c_{2y} + c_{1y}k_{2y} + k_{2y}c_{2y}\right)s + k_{1y}k_{2y}} \tag{2.9}$$

$$Y_2(s) = \frac{k_{2y}F_d(s)}{m_1(m_2+m_3)s^4 + \left(c_{1y}(m_2+m_3)+c_{2y}m_1\right)s^3 + \left(c_{1y}c_{2y}+m_1k_{2y}+(k_{1y}+k_{2y})(m_2+m_3)\right)s^2}$$

$$+\left(k_{1y}c_{2y}+c_{1y}k_{2y}+k_{2y}c_{2y}\right)s+k_{1y}k_{2y}$$

(2.10)

where $s = j\omega$ is the Laplace variable. The resonant frequencies of the drive mode can be found by finding the maximum value of the amplitude $Y_1(s)$ or $Y_2(s)$.

For the sense mode motion, m_2 and m_3 are movable to each other and they form a 2-DOF sense oscillator. The system governing equations of the sense mode motion can be expressed as:

$$m_2\ddot{x}_2 + c_{2x}\dot{x}_2 + k_{2x}x_2 = k_{3x}(x_3 - x_2) + F_{c2}(t)$$

(2.11)

$$m_3\ddot{x}_3 + c_{3x}\dot{x}_3 + k_{3x}x_3 = k_{3x}x_2 + F_{c3}(t)$$

(2.12)

Eqn. (2.11) is the system equation for the proof mass m_2. Eqn. (2.12) is the system equation for the proof mass m_3.

Because in the non-resonant gyroscope, m_3 is designed to be smaller than m_2 in order to achieve large sensor sensitivity, the Coriolis force $F_{c3}(t)$ is very small. Neglecting $F_{c3}(t)$ and taking the Laplace transform of Eqn. (2.11) and (2.12), the sense mode motion becomes:

$$X_2(s) = \frac{m_2\left(m_3s^2 + c_{3x}s + k_{3x}\right)2\Omega_z sY_2}{m_2m_3s^4 + \left(c_{2x}m_3 + m_2c_{3x}\right)s^3 + \left(k_{2x}m_3 + k_{3x}m_3 + c_{2x}c_{3x} + m_2k_{3x}\right)s^2 +}$$

$$\overline{\left(k_{2x}c_{3x} + k_{3x}c_{3x} + c_{2x}k_{3x}\right)s + k_{2x}k_{3x}}$$

(2.13)

$$X_3(s) = \frac{k_{3x}m_2 2\Omega_z sY_2}{m_2m_3s^4 + \left(c_{2x}m_3 + m_2c_{3x}\right)s^3 + \left(k_{2x}m_3 + k_{3x}m_3 + c_{2x}c_{3x} + m_2k_{3x}\right)s^2 +}$$

$$\overline{\left(k_{2x}c_{3x} + k_{3x}c_{3x} + c_{2x}k_{3x}\right)s + k_{2x}k_{3x}}$$

(2.14)

The response of the sense mode is similar to that of the drive mode. The resonant frequencies of the sense mode can be found by finding the maximum value of the amplitude $X_2(s)$ or $X_3(s)$.

The steady-state frequency response of the 2-DOF oscillator has two resonance peaks and a relatively flat region in between. The amplitude of the flat region is less vulnerable to the shift of resonant frequencies due to the parameter variations [22]. Therefore, in order to achieve inherent robustness, the non-resonant gyroscope is designed to work in the flat regions of the drive and sense modes. The design objective is to coincide the flat regions of the drive and sense modes to have the maximum operational frequency range. The top trace in Figure 2.3 is the frequency response of the drive mode. The solid line is the response of y_2 & y_3; the dashed line is the response of y_1. The bottom trace is the frequency response of the sense mode. The solid line is the response of x_3 and the dashed line is the response of x_2. In contrast to the resonant gyroscopes, the non-resonant gyroscopes use dynamical amplifications instead of resonance and operate in the overlapped flat regions of the drive and sense modes.
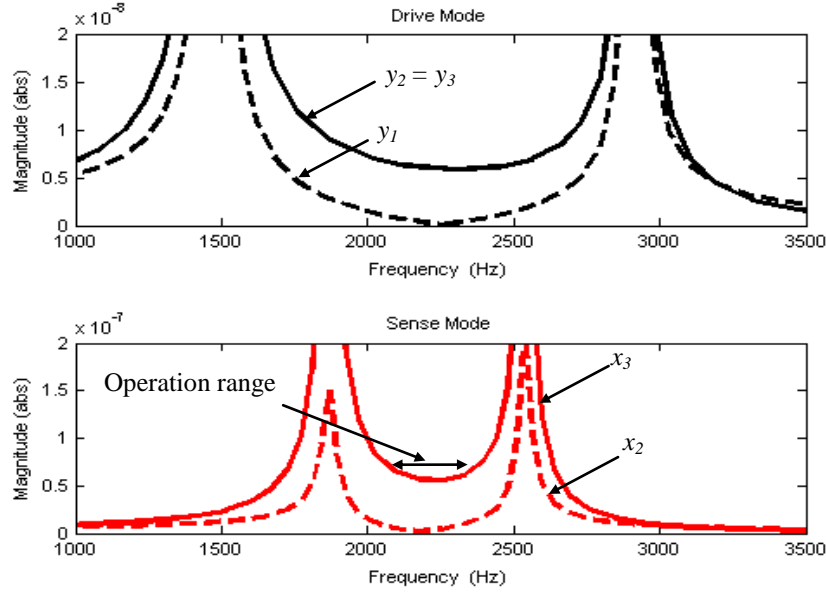
Figure 2.3. Frequency response of the non-resonant gyroscope: (top trace) drive mode and (bottom trace) sense mode.

2.3 Compensator design

The state-space representations of the system model are described by:

$$\begin{cases} \dot{\mathbf{x}} = \mathbf{F}\mathbf{x} + \mathbf{G}u \\ y = \mathbf{H}\mathbf{x} \end{cases} \tag{2.15}$$

where u is the input, y is the output of interest, $\mathbf{x}$ is the state vector, $\mathbf{F}$ is the system matrix, $\mathbf{G}$ is the input matrix, $\mathbf{H}$ is the output matrix. We can determine the matrices $\mathbf{F}$, $\mathbf{G}$, and $\mathbf{H}$ from the system governing equations. The block diagram as shown in Figure 2.4 is defined by the state equations of Eqn. (2.15).
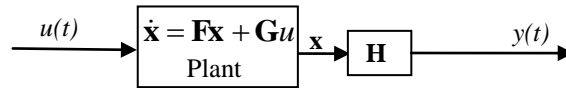
Figure 2.4. Block diagram of the system model in state-space.

23

A compensator in state-space is generally composed of a controller (control law for the closed-loop system) and an estimator (reconstructing all the state variables of a system). One of the most effective and widely used techniques of linear control systems design is the LQR method [30]. The compensator representation is given by:

$$\begin{cases} \dot{\hat{\mathbf{x}}} = \mathbf{F}\hat{\mathbf{x}} + \mathbf{G}u + \mathbf{L}(y - \mathbf{H}\hat{\mathbf{x}}) \\ u = -\mathbf{K}\hat{\mathbf{x}} + \overline{N}r \end{cases} \tag{2.16}$$

where r is the reference input. $\mathbf{K}$ is the controller gain, $\mathbf{L}$ is the estimator gain, $\hat{\mathbf{x}}$ is an estimate state of $\mathbf{x}$, $\overline{N}$ is the gain factor, which is the inverse of the closed-loop DC gain. Based on Eqn. (2.15) and Eqn. (2.16), the block diagram of the LQR closed-loop system is shown in Figure 2.5. The control law allows designers to assign an array of controller pole locations that highly correlate with the system response. For LQR problems, the control law is given by linear-state feedback. The controller poles often dominate the system dynamics. Estimator poles are usually arranged far away from the origin to reduce their influence on the system.
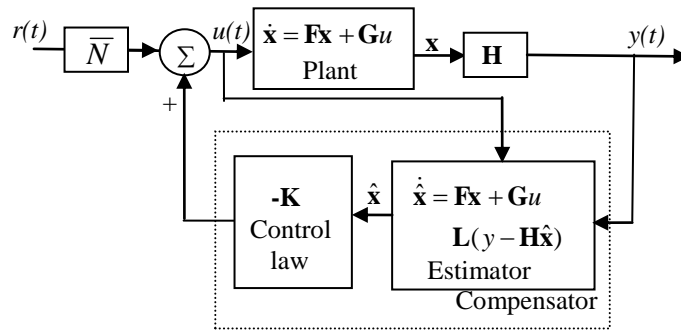
Figure 2.5. Block diagram of state-space design elements.

2.3.1 Calculation of gains

Because the characteristic equation of the closed-loop system is:

24

$$\det[s\mathbf{I} - (\mathbf{F} - \mathbf{GK})] = 0 \qquad (2.17)$$

If the desired locations are known as $s = s_1, s_2, ..., s_n$, then the corresponding desired control characteristic equation is:

$$\alpha_c(s) = (s - s_1)(s - s_2)...(s - s_n) = s^n + \alpha_1 s^{n-1} + \alpha_2 s^{n-2} + ... + \alpha_n \qquad (2.18)$$

The controller gain $\mathbf{K}$ is found by matching the coefficients in Eqn. (2.17) and Eqn. (2.18) and s_i are the controller poles.

The same method can be used to determine the estimator gain $\mathbf{L}$. Because the characteristic equation of the estimator error is:

$$\det[s\mathbf{I} - (\mathbf{F} - \mathbf{LH})] = 0 \qquad (2.19)$$

If the desired location of the estimator error poles as $s = \beta_1, \beta_2, ..., \beta_n$, then the desired estimator characteristic equation is:

$$\alpha_e(s) = (s - \beta_1)(s - \beta_2)...(s - \beta_n) \qquad (2.20)$$

The estimator gain $\mathbf{L}$ is found by comparing the coefficients in Eqn. (2.19) and Eqn. (2.20) and β_i are the estimator poles.

Calculating the gains using this technique is straightforward but tedious when the order of the system is higher than three. An alternative method to calculate $\mathbf{K}$ and $\mathbf{L}$ is given by Ackermann's formula [30, 31]:

$$\mathbf{K} = \begin{bmatrix} 0 & \cdots & 0 & 1 \end{bmatrix} C^{-1} \alpha_c(\mathbf{F}) \qquad (2.21)$$

where $C = [\mathbf{G} \ \ \mathbf{FG} \ \ \mathbf{F}^2\mathbf{G} \ ... \ \mathbf{F}^{n-1}\mathbf{G}]$ and $\alpha_c(\mathbf{F})$ is defined as:

$$\alpha_c(\mathbf{F}) = \mathbf{F}^n + \alpha_1 \mathbf{F}^{n-1} + \alpha_2 \mathbf{F}^{n-2} + ... + \alpha_n \qquad (2.22)$$

where α_i is the coefficient of the desired characteristic polynomial Eqn. (2.18).

$$L = \alpha_e(\mathbf{F})O^{-1}\begin{bmatrix} 0 \\ 0 \\ \vdots \\ 1 \end{bmatrix}$$

(2.23)

where $O = [\mathbf{H} \quad \mathbf{HF} \quad \ldots \quad \mathbf{HF}^{n-1}]^{\mathrm{T}}$ and the coefficients of $\alpha_e(\mathbf{F})$ are the coefficients of the desired characteristic polynomial of Eqn. (2.20).

After determining $\mathbf{K}$ and $\mathbf{L}$, the closed-loop system equations based on Eqn. (2.15) and Eqn. (2.16) become:

$$\begin{cases} \dot{\mathbf{x}}_{cl} = \mathbf{A}_{cl}\mathbf{x}_{cl} + \mathbf{B}_{cl}r \\ y = \mathbf{C}_{cl}\mathbf{x} + \mathbf{D}_{cl}r \end{cases}$$

(2.24)

where $\mathbf{x}_{cl} = \begin{bmatrix} \mathbf{x} & \hat{\mathbf{x}} \end{bmatrix}^{\mathrm{T}}$, $\mathbf{A}_{cl} = \begin{bmatrix} \mathbf{F} & -\mathbf{GK} \\ \mathbf{LH} & \mathbf{F} - \mathbf{GK} - \mathbf{LH} \end{bmatrix}$, $\mathbf{B}_{cl} = \begin{bmatrix} \mathbf{0} \\ G\bar{N} \end{bmatrix}$, $\mathbf{C}_{cl} = [\mathbf{H} \quad \mathbf{0}]$, and

$\mathbf{D}_{cl} = [0]$. Because the controller poles often dominate the system dynamics and the estimator poles are usually arranged far away from the origin, the performance of the closed-loop system is determined by the selected controller poles.

CHAPTER THREE

ANLYSIS AND MODELING OF A RESONANT GYROSCOPE

Typical MEMS simulation mainly focuses on device performance without considering fabrication capabilities and packaging integratibility. This practice often leads to an inefficient product development cycle and increases the cost. This chapter presents an integrated simulation workflow that incorporates the modeling of fabrication process, design analysis, and packaging through a case study of a MEMS tuning-fork gyroscope using CoventorWare. The multi-level simulation has been demonstrated to be efficient to shorten the development process and improve the device performance, and can be used effectively to optimize the gyroscope system.

3.1 Device modeling

The typical structure of a tuning-fork gyroscope is shown in Figure 3.1 [9]. The gyroscope consists of two anchors, four suspension beams, two movable parts, four sets of fixed comb fingers, and electrodes on the backside.
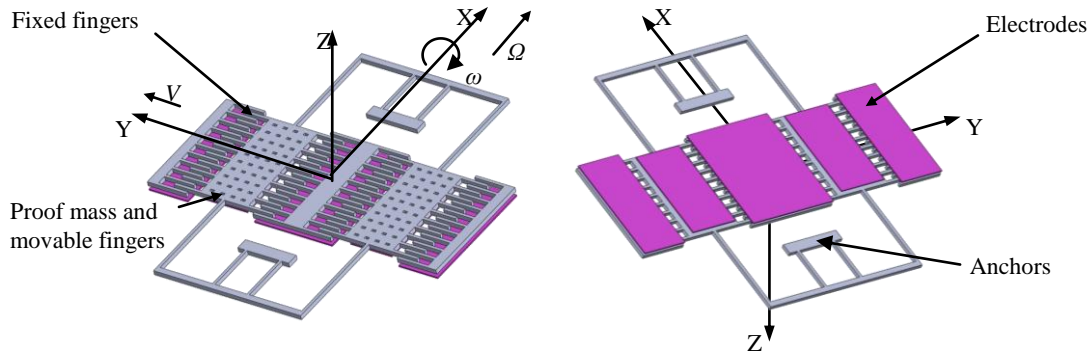
Figure 3.1. The structure of a tuning-fork gyroscope.

The poof mass and movable fingers are excited by the alternating voltage and vibrate with a velocity V along y-axis. The frequency of the alternating voltage is setup at the resonant frequency of the drive mode to achieve maximum amplitude of vibration. Once the gyroscope is subject to an angular rate of ω about x-axis, the Coriolis acceleration will be generated and excites the proof mass into oscillation along z-axis, the sense-mode direction. The Coriolis acceleration is expressed by $2\omega \times V$. The proof mass and electrodes form an array of capacitors. The gap change between the proof mass and the electrode is converted to the capacitance change, which can be detected by using an analog amplifier to demodulate the signal and a low pass filter to recover the motional change signal.

Most traditional MEMS modeling tools focus on the structural behavior without considering the device fabrication process [32, 33]. Ignoring the fabrication capabilities often leads to an inefficient product development cycle and an increased cost. Using CoventorWare, we can create a design model of the tuning-fork gyroscope taking the manufacturability into consideration. Besides the abilities to create 2D layout and 3D structures, the software package allows us to model the realistic deposition and etching steps in the microfabrication process.

Figure 3.2 illustrates the 2D layout of the gyroscope with the dimensions of the initial design labeled. The gap between the proof mass and the electrodes underneath is 3 μm. The small gap increases the damping coefficient of the proof mass due to the squeeze-film effect. Therefore, the proof mass is perforated with etched holes to reduce the out-of-plane damping effect.
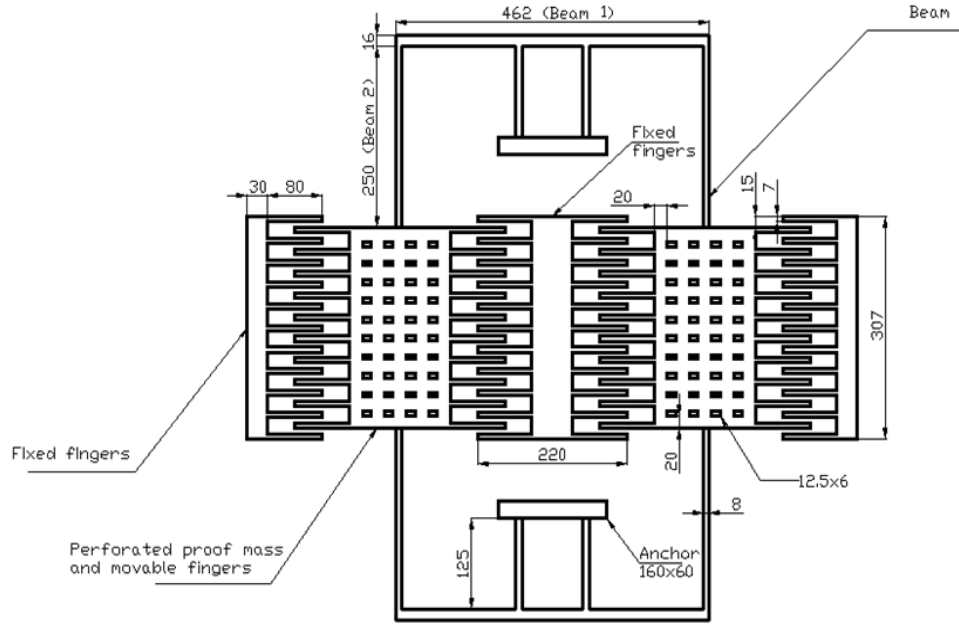
Figure 3.2. The layout of the tuning-fork gyroscope (Unit: μm).

Table 3.1. Fabrication steps for the gyroscope.

Step No.	Process Name	Material	Thickness (μm)
1	Substrate	Silicon	20
2	Deposit Insulator	Silicon Nitride	0.5
3	Deposit to Create Electrodes	Polysilicon	0.5
4	Deposit Sacrifice layer	Polymide	3
5	Etch Anchor Positions	Polymide	3
6	Conformal Deposit for Gyroscope	Silicon	20
7	Etch to Create Gyroscope	Silicon	20
8	Etch to Create Perforations	Silicon	20
9	Remove Sacrifice Layer	Polymide	3

Table 3.1 summarizes the fabrication steps, material selections and the corresponding film thicknesses. Figure 3.3 illustrates the key steps of the process modeling. A silicon wafer is used as the starting material (Figure 3.3(a)). A layer of Si_3N_4 is deposited on the substrate as the insulation film. Next, a layer of polysilicon is deposited on the surface and patterned as electrodes by lithography (Figure 3.3 (b)). A polymide film is coated on the substrate as the sacrificial material. After opening windows for the anchors and fixed fingers by lithography and selective etching (Figure 3.3 (c)), the entire device surface is covered by a thick layer of silicon which is used as the structural material for both the movable parts and fixed structures (Figure 3.3 (d)). Next, the silicon layer is selectively etched to generate the structures and perforations on the proof mass (Figure 3.3 (e)). The final step is to remove the sacrificial layer and release the movable structures (Figure 3.3 (f)).
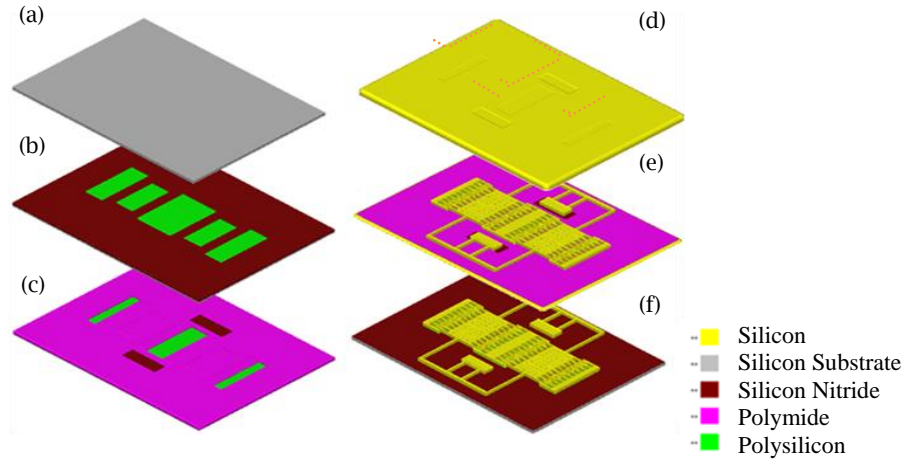
Figure 3.3. Fabrication process modeling of the gyroscope.

3.2 Device performance simulation

3.2.1 Modal analysis

Using the CAD geometry created from the process modeling, we perform the FEM to extract the resonant frequencies and mode shapes from the MEMS gyroscope. The three key vibration responses related to the device's operation are obtained with CoventorWare and are shown in Figure 3.4, where the displacements are exaggerated by ten times. Figure 3.4(a) illustrates the vibration mode in the x-direction for an in-plane gap closing motion between finger sidewalls. The resonant frequency for the X mode is found to be around 185.1 kHz. The driving mode for the in-plane vibration in the y-direction shown in Figure 3.4 (b) has a corresponding resonant frequency of 73.7 kHz. The sensing mode for the out-of-plane vibration in z-direction is shown in Figure 3.4 (c), which has a resonant frequency of 37.98 kHz. The large difference in resonant frequencies between the driving Y mode and the sensing Z mode implies the necessity of design change for performance improvement.

(a) X mode, finger gap closing   (b) Y mode, along the fingers

Modal Displacement Mag.: 0.0E+00   3.1E-01   6.2E-01   9.3E-01   1.2E+00
um   37983.2 Hz   COVENTOR
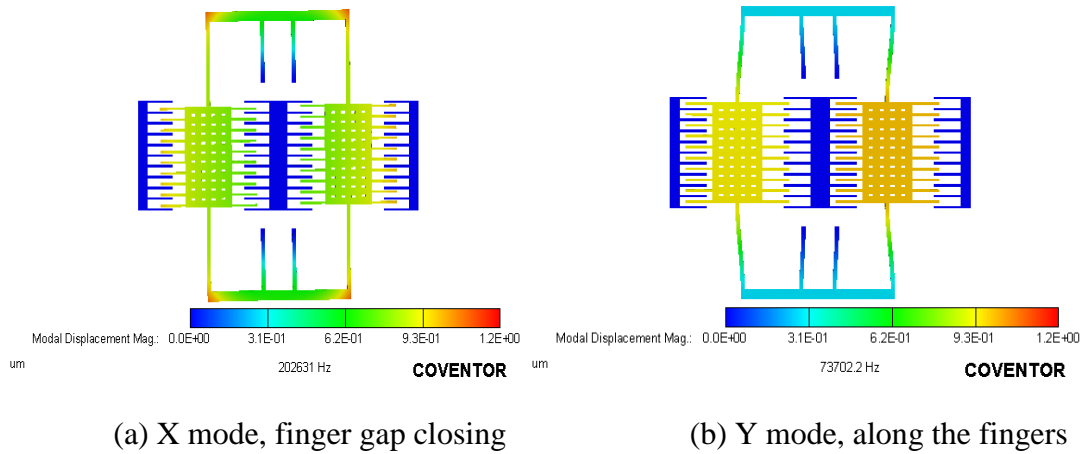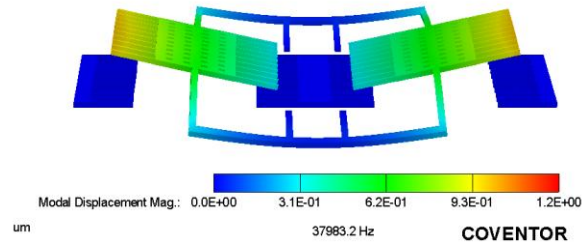
(c) Z mode, vertical to the plate

Figure 3.4. The three major vibration mode shapes.

3.2.2 Frequency response analysis

To understand the device's frequency characteristics, we conduct the frequency response analysis by assembling a behavior model of the system using the Architect module in CoventorWare. The behavior model enables quick what-if analyses of the device under various mechanical and electrical stimuli. Solutions can be obtained with comparable accuracy to that of the finite element simulation, which requires a full-size problem to be solved at each frequency point. Figure 3.5 shows the behavior model of the MEMS gyroscope with illustrations of the 3D physical geometry mapped to the corresponding behavior symbols.

a. Anchor   **b**. Beam   **c**. L-beam   **d**. Proof mass and movable fingers
e. Electrodes underneath the proof mass   **f**. Fixed fingers
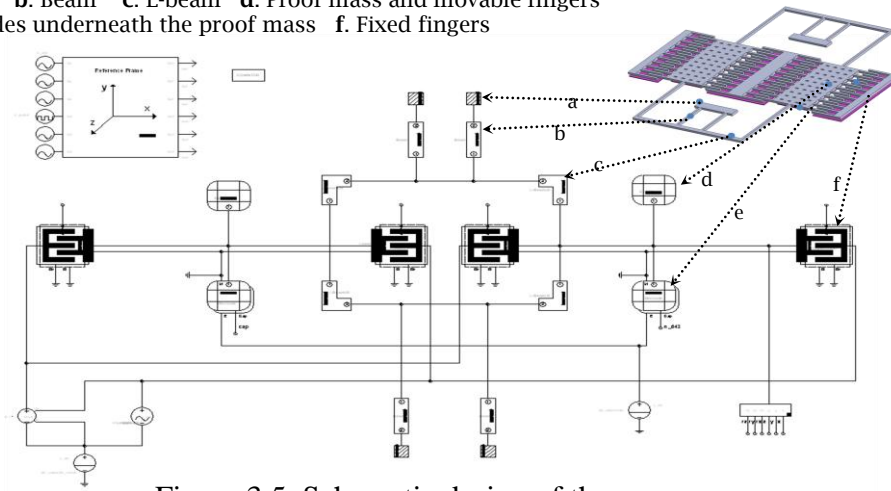
Figure 3.5. Schematic design of the gyroscope.

The behavior symbols are selected from CoventorWare parametric component libraries for MEMS. Each symbol takes a few inputs such as size and position parameters based on the 3D design geometry. They are connected with each other via knots to generate a system schematic diagram. The complicated mathematical descriptions for detailed physical models are reduced to a small number of degrees of freedom for the symbolic models in the schematic description. As a result, complex MEMS involving multiple physical domains and peripheral subsystems can be studied with ease at a high level of abstraction. As the highest resonant frequency among the three modes of interest here is less than 200 kHz, the analysis is performed in a frequency range from 0 to 200 kHz. The simulation is finished in less than 10 seconds. Figure 3.6 shows the frequency response of the MEMS gyroscope.
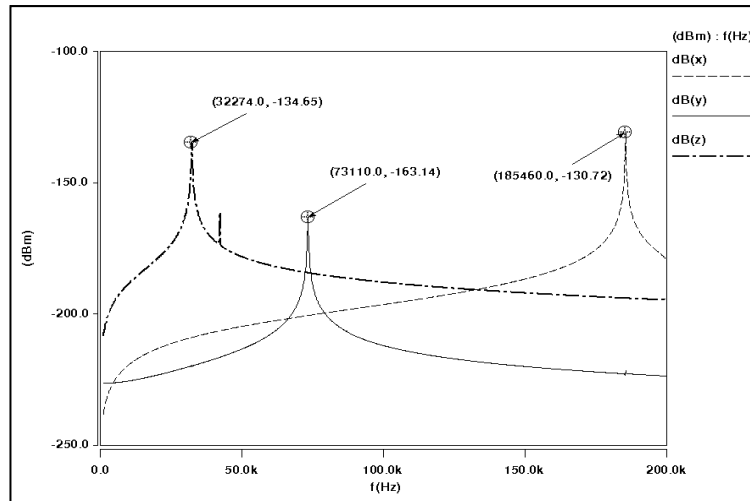
Figure 3.6. Resonant frequency response of the gyroscope.

Table 3.2. Simulation result comparison of Architect and FEM.

	X mode (Hz)	Y mode (Hz)	Z mode (Hz)
Architect	185460.0	73110.0	32274.0
FEM	202631.0	73702.2	37983.2

From Figure 3.6, we observe that the frequency curves peak at 185.5 kHz for the X mode, 73.1 kHz for the Y mode, and 32.3 kHz for the Z mode, respectively. Table 3.2 compares the results by Architect and FEM. The two simulation methods show slight difference. The difference between FEM and Architect might be explained by the assumptions of the beam components made by Architect. Architect approximates the mathematical description of a single beam based on Bernoulli Beam theory [34], which gives accurate results for long and slender beams. Also, beam torsion (Z mode) requires a higher mesh density than that of beam translation (X and Y modes) for accurate results. For preliminary investigation purposes, a simple mesh was created, but mesh convergence studies are always recommended in order to gauge the accuracy of the results. Both the Architect and the FEM results confirm that the driving Y mode and the sensing Z mode have a very weak correlation in the current design. To achieve optimum sensitivity, it is desirable that the two resonant frequencies be as close as possible. Therefore, adjusting some key design parameters and configurations is needed for design optimization.

3.2.3 Design optimization

Since the resonant frequency is a function of the structural stiffness, adjusting the suspension beam dimensions can effectively change the beam stiffness hence the resonant frequency. Our first effort is to change the width of Beam 1, as shown in Figure 3.2, to determine the optimum conditions. The frequency response of the structure with various beam widths is shown in Figure 3.7. The width of the beam is adjusted from 8 to 24 μm with a 4 μm increment. The frequency responses for all three modes show the

same tendency: wider beams have higher resonant frequencies. However, the resonant frequency shift ranges are different: the X mode has the largest shift and the Z mode has the smallest one. Decreased beam width leads to better coupling between Y and Z modes; but it also leads to a smaller resonant frequency of the X mode. As a result, the choice of the Beam 1 width is a tradeoff between the Y-Z mode correlation and the location of X mode resonant frequency.

(a) Y and Z modes   (b) X mode
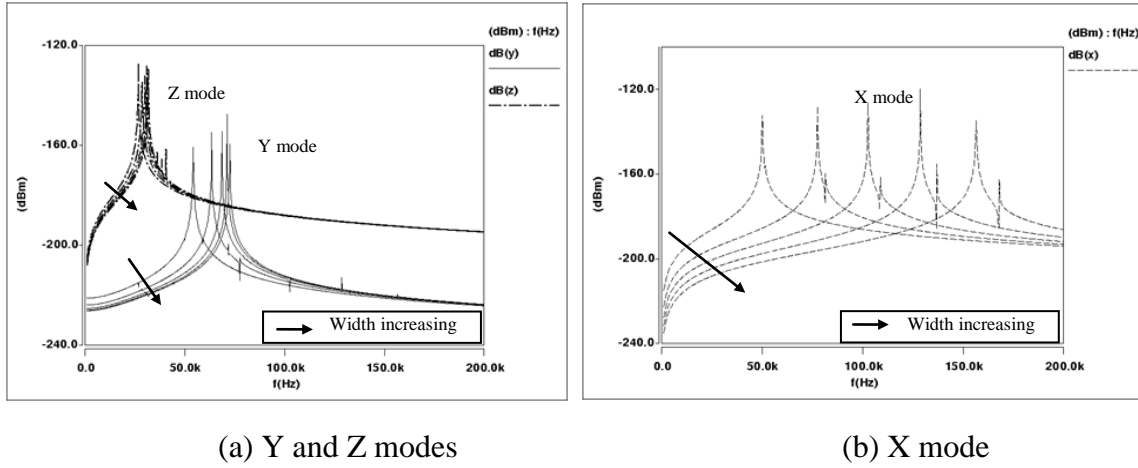
Figure 3.7. Effect of Beam 1 width on the resonant frequencies.

The same optimization process is applied to the Beam 2. Figure 3.8(a) shows the results. The beam width is adjusted from 4 to 16 μm with a 4 μm increment. The resonant frequencies of the structure in all three modes are dependent on the beam width: wider beams have higher resonant frequencies. In contrast to relatively small changes of the Z and X modes, the frequency change of the Y mode has a much wider range from 15 to 100 kHz. With a 4 μm beam width, the Y and Z modes have similar resonant frequencies and the X mode has a much higher one. However, the 4 μm feature size brings challenges to the device fabrication and material selection, which often lead to an increased cost.

Therefore, adjusting beam width is proved to be beneficial in some aspects but deleterious in others.

The effect of the length of Beam 2 on the resonant frequencies of all three modes is shown in Figure 3.8(b). The beam width is fixed at 4 μm and the length is adjusted from 250 to 400 μm. In general, long beams facilitate the deflection of the proof mass during the vibration. The simulation results indicate that the beam length influences the three modes in the same fashion: a longer beam reduces the resonant frequencies of all three modes. The shift magnitudes for the Y and Z modes are higher than that for the X mode. In another word, as the beam becomes longer the undesired mode, X mode, is moved further away from the desired modes, Y and Z modes. Therefore, longer beams are preferred in our gyroscope design.
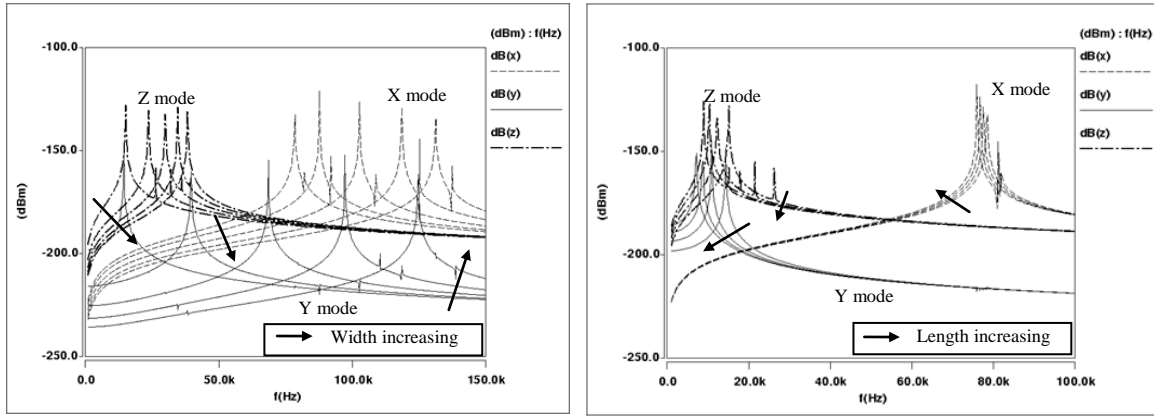
(a) Width effect   (b) Length effect

Figure 3.8. Effect of Beam 2 dimensions on the resonant frequencies.

Combining the results from the initial optimization efforts, the desired geometry of the design can be obtained when Beam 1 is 16 μm by 450 μm and Beam 2 is 4 μm by 400 μm. Figure 3.9 shows the device structure and its frequency response. The suspense

beams have low stiffness and the resonant frequencies for the X, Y, and Z modes are 75.9, 7.2, and 9.0 kHz, respectively.
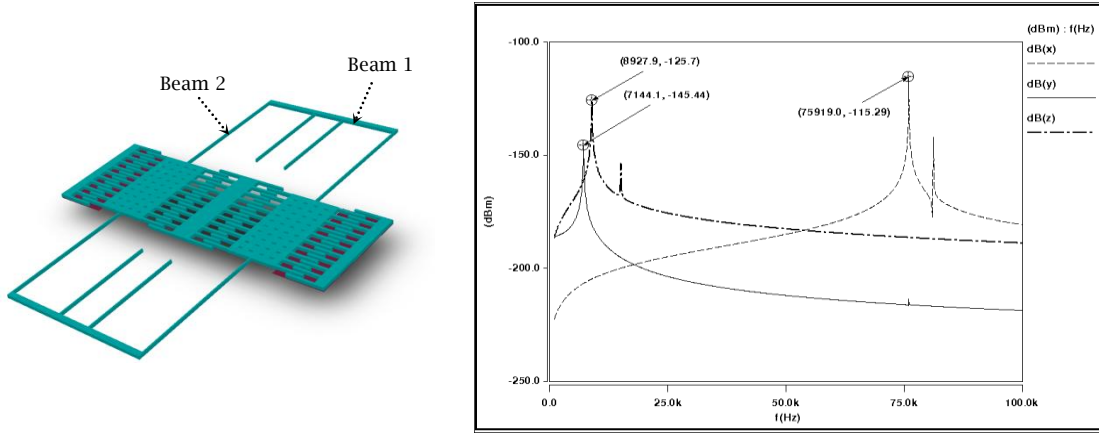
(a) The optimized mode   (b) The improved frequency response

Figure 3.9. Parameter optimization and the corresponding frequency response.

The results demonstrate a good coupling between the driving Y mode and the sensing Z mode. However, this optimized design is not suitable for device miniaturization. The device with the 400 μm long beam is difficult to fit in compact packages. The 4 μm features often require extra constraints and increase the cost of the fabrication process. Moreover, the performance of the device may be easily affected by the environmental factors such as deformation of the package and temperature drift.

In order to achieve both a low stiffness and miniaturization of the device, folded-beam design is incorporated. The folded beam model can be easily generated by inserting the highlighted components into the original design (Figure 3.10). The design parameters are: Beam 1 is 20 μm by 450 μm, Beam 2 is 6 μm by 250 μm, the folded structure is 10 μm by 187.5 μm. The results show that the resonant frequencies of the X, Y, and Z modes are 77.3, 20.6, and 18.1 kHz, respectively.
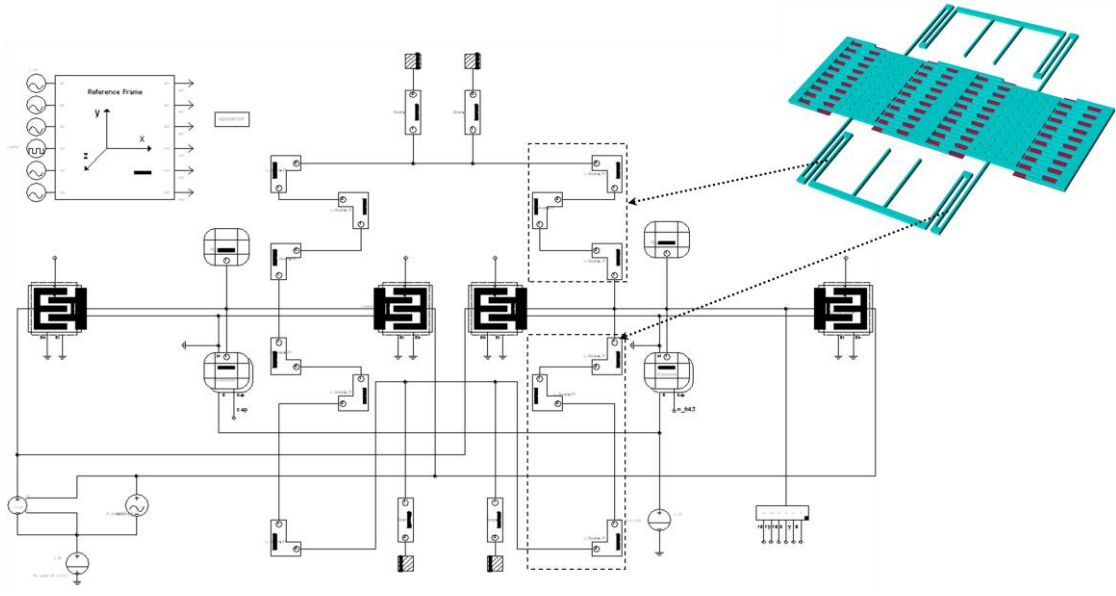
Figure 3.10. Schematic model of the folded-beam gyroscope.
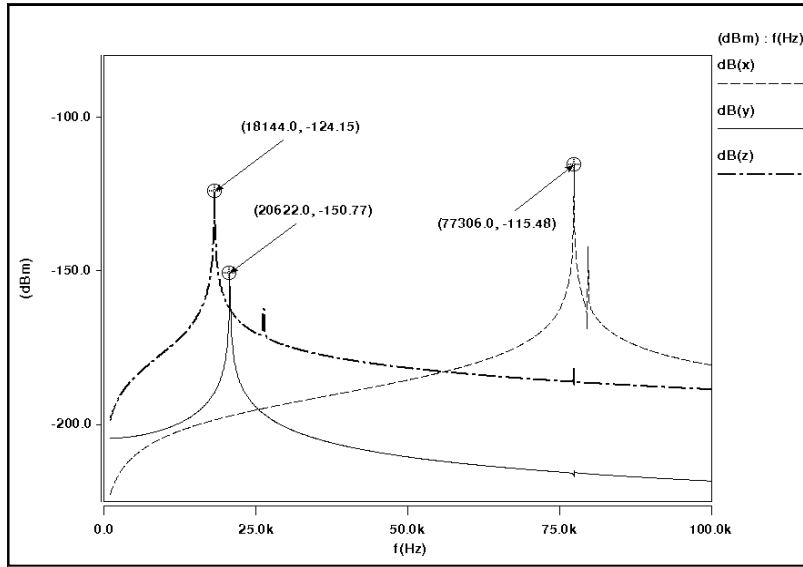
Figure 3.11. Frequency response of the optimized folded-beam design.

The folded-beam design demonstrates high performance which is similar to the original long-beam design. It is also more compact and easier for miniaturization purposes. Furthermore, the smallest feature of the new design is 6 μm, 50% more than the

38

initial design; this can greatly reduce the fabrication complexity and the cost of the final device.

3.2.4 Design sensitivity and Monte Carlo analysis

Geometry variations are inevitable in any microfabricated devices. A design sensitivity analysis is conducted to show how parameter perturbation affects the resonant frequency (20.6 kHz) of the driving Y mode for the folded-beam design. We choose four design parameters from the optimized structure, namely the width and length of Beam 1 and Beam 2. The design sensitivity, defined as the derivative of the resonant frequency with respect to the design parameter, is obtained with CoventorWare. Table 3.3 shows the impact of the parameter perturbation on the Y mode resonant frequency.

Table 3.3. Influence of parameter perturbation on the Y mode resonant frequency (20.6 kHz).

	Parameter	Sensitivity	Nominal size (µm)	Perturbation (µm)	Change in Frequency (Hz)
Beam 1	Width	0.019	16	0.2	4.89
	Length	-0.019	450	0.2	-0.19
Beam 2	Width	1.480	6	0.2	1016.3
	Length	-1.470	250	0.2	-24.2

A constant perturbation error of 0.2 µm is assumed for all design parameters, e.g., induced by tolerance in fabrication process. The perturbation is normalized to the nominal value for each parameter. For instance, the width of Beam 2 shows a 3.33%

variation due to the perturbation. The width parameter has a sensitivity of 1.48. When multiplied by the normalized perturbation, the sensitivity yields the normalized change in the resonant frequency, i.e., $3.33\% \times 1.48 = 4.93\%$. In absolute terms, the frequency change due to the width variation can be calculated as $4.93\% \times 20.6$ kHz $= 1016.3$ Hz. The sensitivity analysis unveils the parameters that are most likely to cause frequency drift and performance deterioration, and can be used to guide design decisions early in the development cycle.

The MEMS gyroscope is next studied with Monte Carlo simulation to estimate the uncertainty in mass production due to random variation in design parameters. The four parameters listed in Tab. 3.2 are given a normal distribution around their nominal values. Monte Carlo analysis is carried out on the resonant frequency in the Y direction with 500 sample points. An acceptable driving frequency range is predefined as $\pm3\%$ deviation from the nominal value of 20.6 kHz, i.e., between 20 kHz (lower bound) and 21.2 kHz (upper bound). Figure 3.12 shows the simulated yield results. The top histogram in Figure 3.12 shows the statistical distribution of the resonant frequency in Y direction due to the random variation in the design parameters. The bottom plot in Figure 3.12 gives the measured frequency for each of the 500 sample points. The yield of the mass production is predicted to be 75%, which means 75% of the device samples out of the mass production will have a driving mode resonant frequency within the acceptable frequency range.
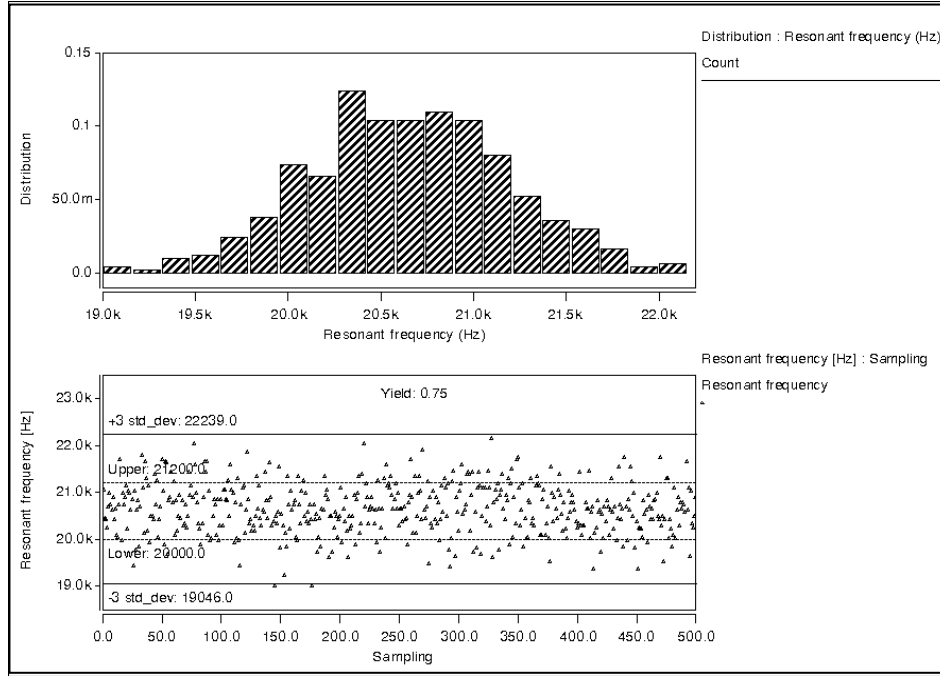
Figure 3.12. Sensitivity analysis for Y mode frequency.

The Monte Carlo analysis reveals the uncertainty propagation, and estimates the yield impact of the design parameter variations. Information derived from the analysis can help bring insights into the fabrication process control to increase the yield of the mass production.

3.3 Package analysis

Gyroscopes do not require a physical contact with the outside world; the package can therefore be hermetically sealed. The package should have little or no influence on the sensor performance; it should not affect the frequency response of the sensor. Of concern here is how the packaged sensor performs in extreme operating conditions with a wide temperature range.

Given the small dimension of the designed folded-beam gyroscope, the sensor is packaged as a surface mounted device (SMD). A package model, SMD_KD_VA3703

41

from the CoventorWare package library, is selected. The lateral dimension of the package is 3.2×2.8 mm^2 and the cavity to contain the sensor is 942×842 μm^2. The gyroscope is mounted on the substrate of the cavity as shown in Figure 3.13. The four pins are fixed on the printed circuit board, and are subject to the temperature loading ranging from -40 °C to 120 °C with an increment of 40 °C. The thermally induced mechanical stress is solved by the FEM and is shown in Figure 3.13.

(a) Top view   (b) Rear view

(c) Deformation at -40 °C   (d) Deformation at 120 °C
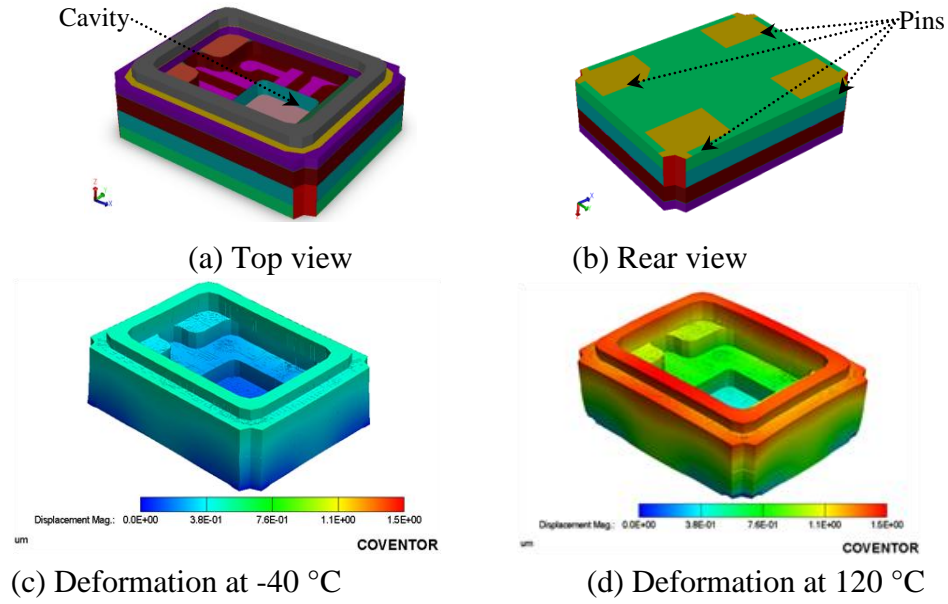
Figure 3.13. Package model and thermal-induced deformation.

The finite element analysis provides the temperature distribution and mechanical deformation of the package. The information can be imported to the system-level modeling to estimate the real-time sensitivity of the gyroscope. The frequency responses of the device at the four different operating temperatures are shown in Figure 3.14. We can see that the resonant frequency decreases as the operating temperature increases. The frequency shift is relatively small though, with a difference less than 100 Hz in the given temperature range. Compared to the fabrication uncertainties, the effect of the temperature-induced package deformation on the resonant frequency is nearly negligible.
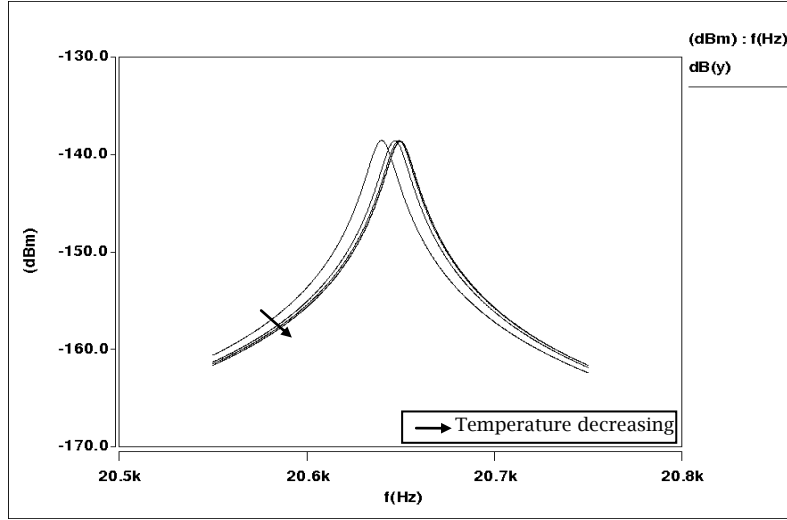
Figure 3.14. Resonant frequencies of the device at various temperatures.

3.4 Discussions and conclusions

This chapter describes an integrated simulation workflow that incorporates the modeling of fabrication process, device design, and packaging through a case study of a MEMS tuning-fork gyroscope using CoventorWare. A MEMS gyroscope design is generated based on mask layout and fabrication process restrictions, and analyzed using finite element and behavior modeling approaches. To increase the driving and the sensing mode correlation for the sensor, the design is optimized through parameter sweeping and configuration modification. A folded-beam design with tailored parameters is proposed to achieve both a low stiffness and compactness for the miniaturized device. Design sensitivity analysis suggests that the device performance is highly sensitive to the suspension beam width. A fabrication-induced variation of 0.2 μm in a beam width can lead to a driving mode frequency shift of over 1000 Hz. With a small sample Monte Carlo analysis, the yield of gyroscope mass production is estimated to be 75%, provided that the acceptable range for the driving frequency is within ±3% deviation from its

43

nominal value. Thermal stress analysis of a SMD package is also performed to model the packaged sensor undergoing extreme temperature variations. Results show that the maximum temperature-induced frequency shift in the MEMS device is less than 100 Hz in a temperature range from -40 °C to 120 °C. The integrated multi-level simulation presented in this chapter demonstrates to be an effective way of optimizing the MEMS device to significantly reduce post-design fabrication cost and improve device performance.

FEEDBACK CONTROL OF A RESONANT MEMS GYROSCOPE

There has been much research to design the sense-loop control of MEMS vibratory gyroscopes. The adaptive control algorithm is investigated in [35, 36]. It enables self-calibration, large robustness to parameter variations, and has no zero-rate output. In [37, 38], H_∞ controllers are used to overcome parameter uncertainties. Since the controllers include the dynamic of the mechanical plant, signal processing filter, and input signal model, their control effort of the controller grows high. In [39], a hybrid algorithm, which takes the merits from adaptive and sliding mode algorithm, is proposed. A control and digital signal processing integrated circuit is used in [40, 41]. The application specific integrated circuit (ASIC) shows great promises for replacing the traditional analog control electronics. It is particularly useful for a higher order controller design. The MEMS gyroscopes with reported feedback design can achieve high robustness to fabrication uncertainties; however, efficient implementation of the feedback remains a big challenge. Proportional-integral-derivative (PID) feedback mechanism is the most widely used in industrial control systems. With the PID controllers, the design system can be easily implemented but the trial-and-error process does not guarantee control optimality [42, 43].

In this chapter, we investigate a lead compensator design for the control of a tuning-fork vibratory MEMS gyroscope using the optimal LQR technique. LQR technique provides optimal closed-loop poles which achieve varying balances between a fast system response and a low control effort. The optimum performance of the controller

45

is obtained with less iterations of trial and error. The resulting lead compensator is physically easy to realize. The compensator designed in MATLAB allows the controlled MEMS gyroscope to achieve user-specified wide bandwidth and small scale factor error. The MEMS device is simulated using behavior models in CoventorWare with the embedded compensator. The closed-loop performance, including linearity, dynamic range, and robustness to fabrication uncertainties as well as noise is analyzed and reported in this chapter.

4.1 Transfer function

The structure of the MEMS gyroscope discussed in this chapter is illustrated in Figure 3.1 [9]. The gyroscope consists of four suspension beams, two proof masses with movable fingers, and four sets of fixed comb fingers.
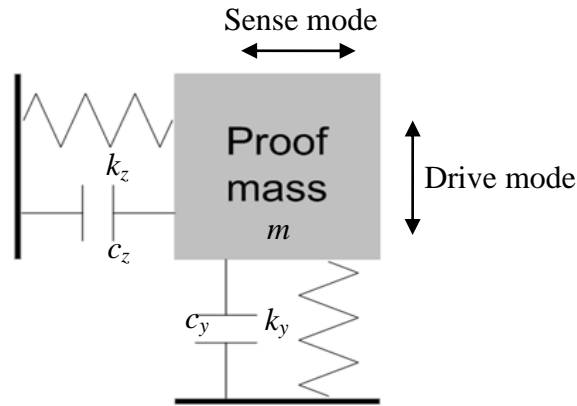
Figure 4.1. Lumped model of the gyroscope.

The motion of the gyroscope can be modeled as a lumped mass-damper-spring system along both the drive-mode direction and the sense-mode direction (Fig. 4.1). The governing equations are given by:

$$\begin{cases} m\ddot{\mathbf{y}} + c_y\dot{\mathbf{y}} + k_y\mathbf{y} = \mathbf{F_y} \\ m\ddot{\mathbf{z}} + c_z\dot{\mathbf{z}} + k_z\mathbf{z} = \mathbf{F_z} + 2m_z\boldsymbol{\omega}\times\mathbf{V} \end{cases} \tag{4.1}$$

where m is the mass, c_y, c_z, k_y, k_z are damping coefficients and spring constants, respectively, in each direction. $\mathbf{F_y}$ is the external driving force, which is usually a sinusoidal excitation. $\mathbf{F_z}$ is the external force which is comprised of parasitic and external inertial forces. In this chapter, we will focus on the design of the sense loop control. The transfer equation of the system along the sense-mode direction can be expressed as:

$$G(s) = \frac{m}{ms^2 + cs + k} \tag{4.2}$$

in which m, c, and k is the proof mass, damping coefficient, and spring constant in the sense-mode direction.

An open-loop gyroscope has limited performance in terms of bandwidth and linearity. Nonlinear effects caused by the damping and the electrostatic forces increase significantly with the deflection of the proof mass [44]. One method of reducing the nonlinearities and improving the performance is force balancing which keeps the proof mass at its original position. Therefore, a force-balancing feedback is designed and a contradictory force is generated to counteract the deflection.

4.2 Compensator design

A compensator in state-space is generally composed of a controller (control law for the closed-loop system) and an estimator (reconstructing all the state variables of a system), as shown in Fig. 4.2.
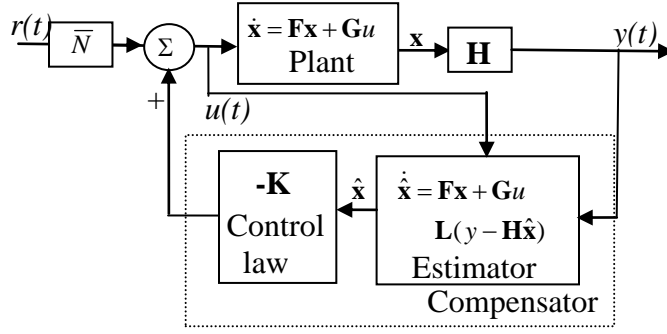
Figure 4.2. Block diagram of state-space design elements.

In Fig. 4.2, $\mathbf{x}$ is the state vector, $\hat{\mathbf{x}}$ is an estimate state of $\mathbf{x}$, $\mathbf{K}$ is the controller gain and $\mathbf{L}$

is the estimator gain. Here, the system matrix $\mathbf{F} = \begin{bmatrix} 0 & 1 \\ -\dfrac{k}{m} & -\dfrac{c}{m} \end{bmatrix}$, the input matrix

$\mathbf{G} = \begin{bmatrix} 0 \\ 2\boldsymbol{\omega} \times \mathbf{v} \end{bmatrix}$, and the output matrix $\mathbf{H} = \begin{bmatrix} 1 & 0 \end{bmatrix}$. The control law allows us to assign an

array of controller pole locations that will highly correlate with system response.

Therefore, the controller poles often dominate the system dynamics. Estimator poles are

usually arranged far away from the origin to reduce their influence on the system. The

LQR problem is to find the control that weights the relative cost of tracking error with

respect to the control effort. The optimal values of $\mathbf{K}$ and $\mathbf{L}$ are those which place the

closed-loop poles at the stable roots of the symmetric root-locus (SRL) equation:

$$1 + \rho G(s)G(-s) = 0 \tag{4.3}$$

where $G(s)$ is the open-loop transfer function. ρ is the weighting factor. After selecting

the controller and estimator poles, we can compute the controller gain ($\mathbf{K}$) and the

estimator gain ($\mathbf{L}$) by Ackermann's formula and substitute them into the following

compensator transfer function [30]:

48

$$D_c(s) = -\mathbf{K}(s\mathbf{I} - \mathbf{F} + \mathbf{GK} + \mathbf{LH})^{-1}\mathbf{L} \qquad (4.4)$$

According to Fig. 4.2, the closed-loop transfer function becomes:

$$CLTF = \frac{G(s)}{1 + D_c(s)G(s)} \qquad (4.5)$$

The general LQR design procedure for the MEMS gyroscope is summarized as follows:

Step 1: Determine the transfer function of the system *G(s)*, the system matrix **F** and the input matrix **G**.

Step 2: Draw the symmetric root locus of *G(s)*.

Step 3: Choose the controller poles to meet the dynamic response requirements.

Step 4: Select the estimator poles which are two to eight times faster than the closed-loop controller poles.

Step 5: Calculate the control gain **K** and the estimator gain **L**.

Step 6: Calculate the transfer function of the compensator by Eqn. (4.4).

Step 7: Determine the controller performance and stability.

Previously, researchers have reported closed-loop gyroscopes with bandwidth of a few thousand hertz [45-47] and scale factor error less than 1% [43, 48]. In this chapter, we are targeting a closed-loop bandwidth BW over 30 kHz and a scale factor error of 1% as our preliminary design specifications. The parameters of the gyroscope and the design criteria of the compensator are listed in Tab. 4.1.

Table 4.1. Design parameters and specifications of the gyroscope.

Parameters	Value	Unit
Proof mass (*m*)	1.3×10^{-9}	kg

Damping coefficient (c)	0.4×10^{-6}	N/(m/s)
Spring constant (k)	30.68	N/m
Bandwidth (BW)	>30	kHz
Scale factor error (ΔS)	<1%	-

The value of the proof mass m, damping coefficient c, and spring constant k are obtained from the corresponding 3D model as shown in Fig. 3.1. The compensator is designed to meet the design specifications. Because the width variation of the suspension beams is the most common source to cause performance deterioration [49], ±10% spring constant variations is assumed for the MEMS device. Inserting Eqn. (4.2) and Eqn. (4.4) into Eqn. (4.5), the closed-loop DC gain becomes:

$$A = |CLTF|_{s \to 0} = \frac{m}{k + mK} \tag{4.6}$$

where K is the compensator gain which is determined from Eqn. (4.4) with s = 0. The scale factor change under spring constant uncertainties can be investigated by:

$$\Delta S = \frac{A_{max} - A_{min}}{A_{max}} = 1 - \frac{\dfrac{m}{k_{max} + mK}}{\dfrac{m}{k_{min} + mK}} \tag{4.7}$$

where $A_{max} = A(k_{min})$, $A_{min} = A(k_{max})$. Therefore, under ±10% parameter variations, the scale factor criterion $\Delta S = 1\%$ with respect to the compensator gain K becomes:

$$K = 18.9 \frac{k}{m} = 4.56 \times 10^{11} \tag{4.8}$$

Use of the state-space approach has often been regarded as modern control design. However, finding the pole locations is critiqued to be less straightforward than

the root-locus design method. We employ SRL plots which assist to find the desired pole locations. From Eqn. (4.3) and (4.8), we can determine the controller pole locations to achieve the desired closed-loop performance.
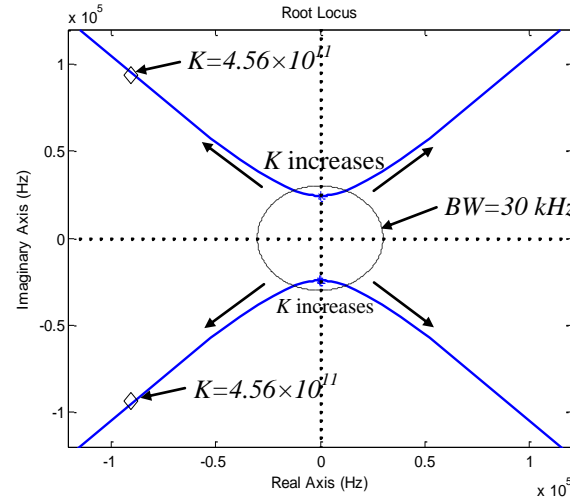
Figure 4.3. Symmetric root locus of the gyroscope.

Figure 4.3 depicts the symmetric root locus of the gyroscope with the design criteria labeled. The solid blue lines are the paths of all possible poles. The circle in dashed line corresponds to a closed-loop bandwidth of 30 kHz. Two diamond markers point out the pole locations that meet the design criterion of $\Delta S = 1\%$ with a corresponding compensator gain K of 4.56×10^{11}. The frequency of the corresponding poles is approximately 130 kHz. Because the compensator gain K increases if the closed-loop poles are selected further away from the open-loop poles, the controller poles, indicated by the diamond markers, are selected to meet the design criteria. The estimator poles are selected to be eight times faster than the controller poles in order to reduce the influence on the entire system. With the closed-loop poles, the control gain **K** and estimator gain **L** are determined by using Ackermann's formula. The compensator transfer function that results from Eqn. (4.4) becomes:

$$D_c(s) = \frac{K(Ts+1)}{(O(s_2) + \alpha Ts + 1)} \tag{4.9}$$

For our gyroscope design, the coefficient of the second order is orders of magnitude smaller than that of the first order. Ignoring second order term, the transfer function is simplified as the standard format of a lead compensator:

$$D_1(s) = \frac{K(Ts+1)}{(\alpha Ts + 1)} \tag{4.10}$$

The values of K, T, and α are 4.56×10^{11}, 2×10^{-6} and 0.1 respectively based on the LQR design. To validate the compensator design, the open-loop and the closed-loop Bode plots of $D_1(s)G(s)$ are generated. The resulting phase margin is 53° (Figure 4.4.(a)). LQR design achieves the maximum phase margin from the compensator without the trial-and-error process. The closed-loop bandwidth is approximately 130 kHz (Figure 4.4.(b)), which meets the bandwidth requirement.
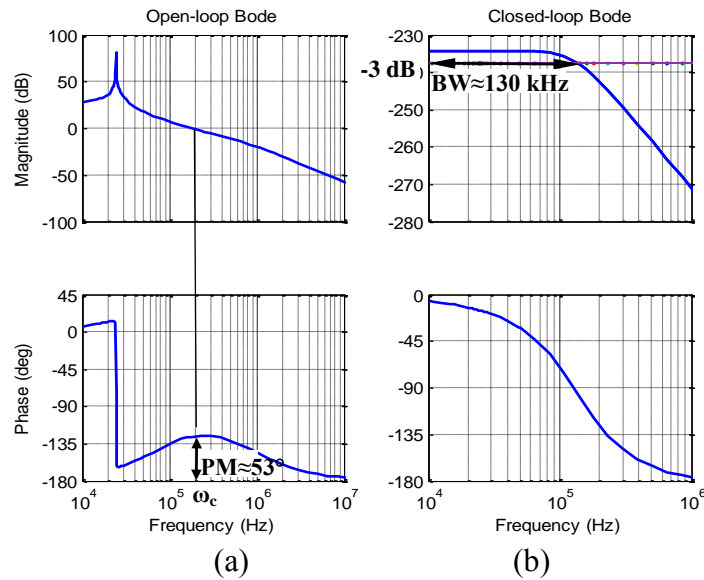

Figure 4.4. Bode plot: (a) open loop and (b) closed loop.

4.3 Closed-loop system modeling

To understand its characteristics, the MEMS gyroscope is studied by behavior models using Architect suite in CoventorWare. The behavior-model approach provides swift analyses of the device under the mechanical and electrical stimuli. Figure 4.5 illustrates the schematic design of the closed-loop MEMS gyroscope. The components in the schematic model the mechanical and electronic behaviors of the gyroscope. Component A in the schematic layout is the reference frame which is used to apply accelerations and angular velocities relative to the reference coordinate system. Component B is the Coriolis acceleration input. Component C is the control gain. It reverses the sign of the signal to achieve the negative feedback. Component D is the transfer function of the compensator. Component E is the interface for the conversion of translational position signals to no-unit control signals [34]. Component F is the bus connectors. It is used to probe translational position signals. The rest of the components include various beams, anchors, rigid plates, electrodes, comb fingers, signal sources, as listed in Tab. 4.2.

Table 4.2: Components used in the schematic layout.

	Beam		Fixed fingers
	L-beam		Alternating voltage
	Anchor		DC voltage
	Rigid plate and movable fingers		Electrodes

A: Reference frame

B: Coriolis acceleration input

C: Negative feedback

D: Compensator

E: Translation to *var* interface

F: Bus connectors
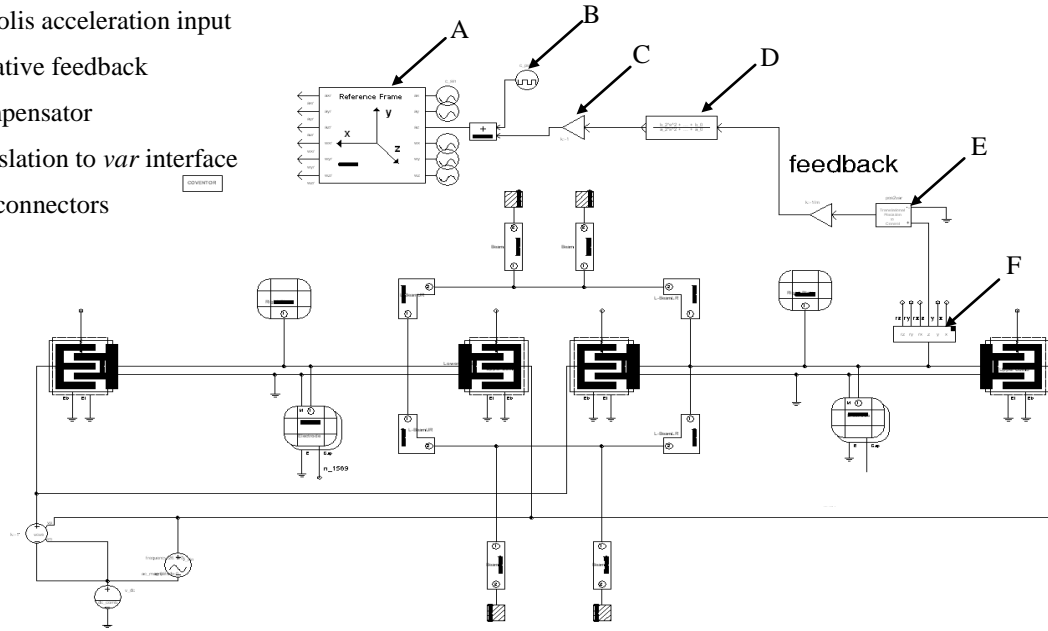
Figure 4.5. Schematic design of the closed-loop gyroscope.

4.4 Simulation results

To understand the time response of the operating gyroscope, the transient analysis is performed by behavior-model approach in CoventorWare. Figure 4.6 compares the open-loop and closed-loop response under the same input. The top trace is square wave Coriolis acceleration input with an amplitude of 1 m/s^2 and a period of 20 ms. The middle and bottom traces are the open-loop and closed-loop responses of the proof mass, respectively. The open-loop system settles at approximately -40 pm, which meets the analytical value m/k = 42.65 pm. The closed-loop system has a much shorter settling time and a less overshoot; the system settles at approximately 2.0 pm which meets the closed-loop DC gain of $\dfrac{m}{k+mK}$ = 2.08 pm given by Eqn. (4.6).
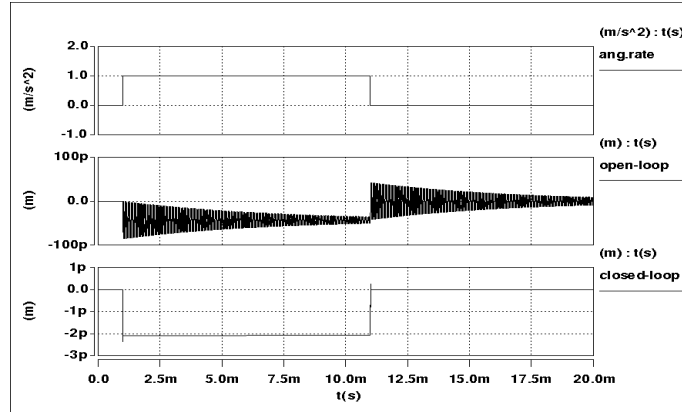
Figure 4.6. Simultion results of the gyroscope: (top trace) step input, (middle trace) step

response of the open-loop system, and (bottom trace) step response of the closed-loop

system.
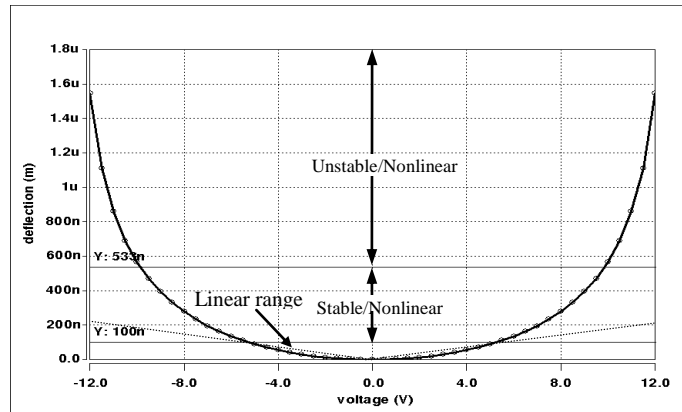
Figure 4.7. Deflection of the proof mass versus required bias voltage of the feedback

electrostatic force.

Figure 4.7 plots the required bias voltage of the feedback electrostatic force to

counterbalance different deflections. In the small deflection region, the bias voltage is

linearly proportional to the deflection. However, if the proof mass is deflected further, the

feedback relationship becomes non-linear. The figure shows that the linear range is

approximately in between ±100 nm. Because the gap between the proof mass and the

55

electrode is designed as 1.6 μm, the analytic stable deflection range is 1.6 μm/3 ≈ 533 nm. Beyond this range, the system is unstable due to the pull-in effect, when the electrostatic force is greater than the spring's restoring force [50].

The open-loop gyroscope is designed to work at the resonant frequency of the sense mode. Figure 4.8 draws the open-loop calibration rate plot, showing the deflection response for different angular rate input at the resonant frequency. The sensitivity can be defined as the derivative of the output change with respect to the input. The deflection-change equivalent sensitivity is 17.6 nm/(m/s^2). As mentioned earlier, the stable range is 533 nm and the linear range is 100 nm. Therefore, the maximum input falling in the stable linear range is 5.67 m/s^2 as marked in Fig. 4.8.
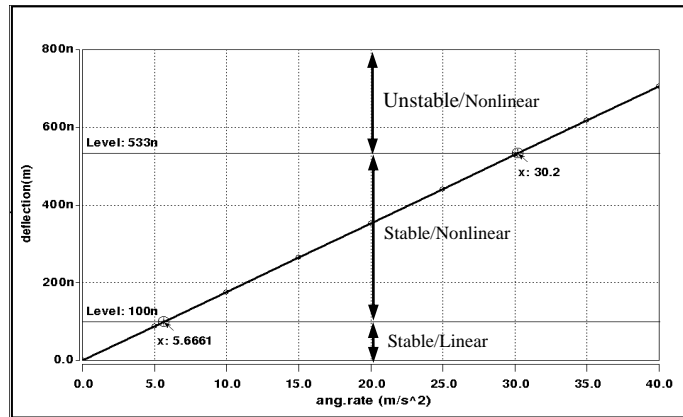
Figure 4.8. Open-loop calibration rate plot, showing amplitude output versus angular rate input.

The closed-loop gyroscope is designed to operate at any frequency in the closed-loop bandwidth. Figure 4.9 shows the closed-loop calibration rate plot at 1000 Hz. The functional gyroscope is in the stable linear range under 40 m/s^2 input. Because the deflection of the proof mass is much smaller than 100 nm linear range limit, the closed-loop gyroscope is capable of detecting the input larger than the open-loop gyroscope.

Therefore, the closed-loop gyroscope expands the detectable Coriolis acceleration range. The simulation shows that the deflection-change equivalent sensitivity of the closed-loop gyroscope is 2.1 pm/(m/s^2). Although the sensitivity is smaller than for the open-loop device, it can be increased with the various gain settings in the circuit [44].
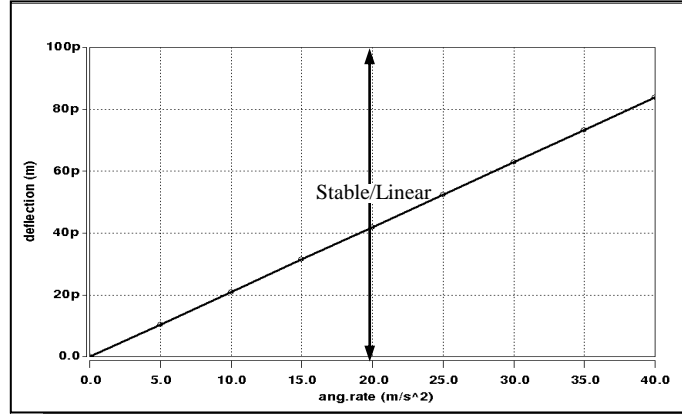
Figure 4.9. Closed-loop calibration rate plot, showing amplitude output versus angular rate input.

The noise degrades the resolution of the gyroscope. The white noise with a power spectral density of 5.58×10^{-8} is added on the input signal as shown in the top trace of Fig. 4.10. The open-loop and closed-loop output are shown in the middle and bottom trace, respectively. The mean deflection for the open-loop is -39.54 pm with a standard deviation of 14.91 pm and the mean deflection for the closed-loop is -2.07 pm with a standard deviation of 0.1 pm. The results confirm that the proposed lead compensator is able to prevent the angular rate measurement from being interfered by the noise.
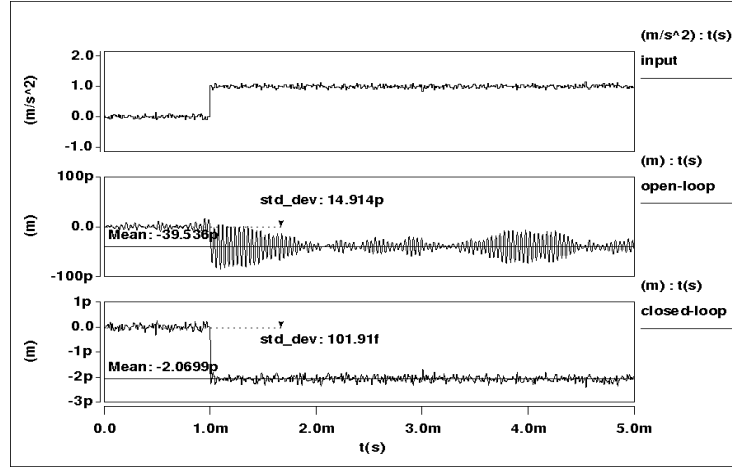
Figure 4.10. Simultion results of the effect of noise on the gyroscope: (top trace) step input with the noise, (middle trace) response of the open-loop system, and (bottom trace) response of the closed-loop system.

Figure 4.11 shows the scale factor error of the open-loop gyroscope under ±10% parameter variations. Under the step input, the nominal value of the output is -39.64 pm. +10% and -10% perturbation ratios lead to the steady-state values of -36.25 and -44.21 pm, respectively. According to the definition, the scale factor error is over 18% for the open-loop gyroscope.
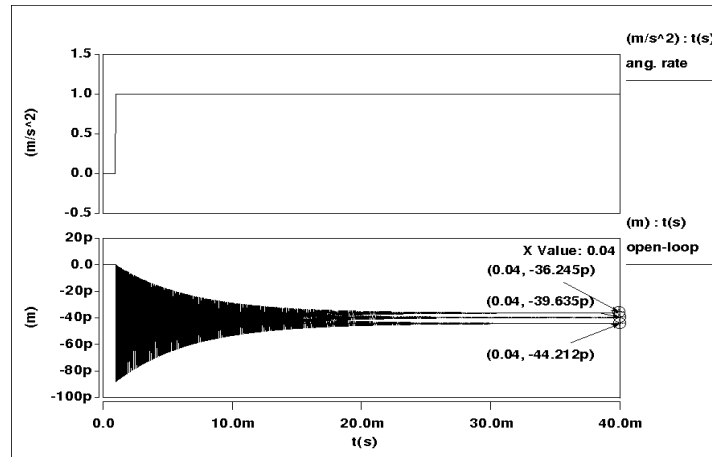
Figure 4.11. (Top trace) step input and (bottom trace) step response of the open-loop

gyroscope under ±10% parameter variations.

To clearly observe the scale factor change of the closed-loop gyroscope, the response is magnified in Fig. 4.12. The nominal value of the output is -2.07 pm. The perturbation results in a 0.7% error by using the compensator design. The result is similar to the PID controller designs reported in [43, 48]. Compared to an 18% open-loop scale factor uniformity error, the results show that the closed-loop gyroscope is less sensitive to the parameter perturbations.
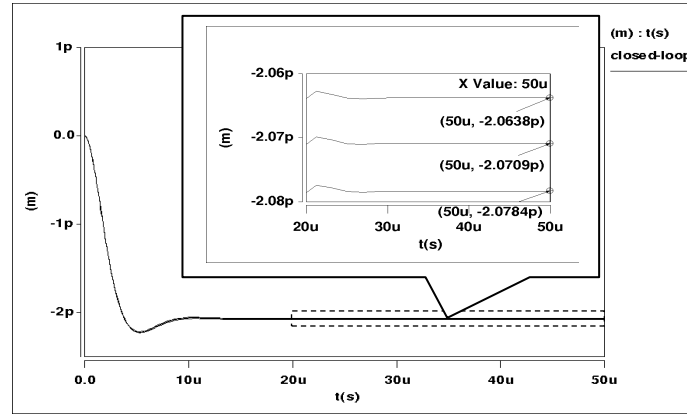
Figure 4.12. Step response of the closed-loop gyroscope under ±10% parameter

variations.

4.5 Discussions and conclusions

In this chapter, a lead compensator is designed by LQR technique for a MEMS gyroscope. LQR well balances the control effort and system response. The resulting compensator is less sensitive to changes in the plant. Lead compensator is easy to physically implement with electronic circuits. With this efficient compensator design, our simulation results show that the closed-loop gyroscope can achieve high linearity, wide

59

dynamic range, and high robustness to parameter and environment uncertainties. The robustness analysis shows that under ±10% perturbation ratio, the scale factor uniformity error is 0.7%, which is comparable with the controller designed in other research. The investigation presented in this chapter demonstrates that the LQR is an effective design to control MEMS gyroscopes.

CHAPTER FIVE

ANALYSIS AND MODELING OF A NON-RESONANT GYROSCOPE

This chapter analyzes and optimizes a 4-DOF non-resonant gyroscope design by using behavior model approach. Compared to traditional FEM, the behavior model method can significantly shorten the simulation time with relatively high accuracy; and it is proven to be a powerful tool for MEMS gyroscope design. The damping in the MEMS device is extracted and used as macromodels in CoventorWare. The results are verified by the analytical equations. With optimum configuration and damping, the frequency response shows that the 4-DOF non-resonant gyroscope has a wide bandwidth and it is less sensitive to the variation in parameters.

5.1 Device modeling

The same as most reported MEMS gyroscopes, the 4-DOF gyroscope measures the angular velocity based on the Coriolis effect [9]. Figure 5.1 shows the schematics of the gyroscope. An alternating voltage is applied to the fixed drive comb fingers. The sinusoidal electrostatic force is generated to drive the proof masses into oscillation along Y-axis, the drive-mode direction. When the gyroscope starts to rotate at a rate of Ω along Z axis, the device is subject to the Coriolis force which oscillates m_2 and m_3 along X-axis, the sense-mode direction. The movable fingers attached to m_3 and the fingers fixed on the silicon substrate form a group of parallel-plate capacitors. The gap change between the fingers leads to the capacitance change that can be detected by the electronic circuit. Therefore, the angular rate Ω can be detected.
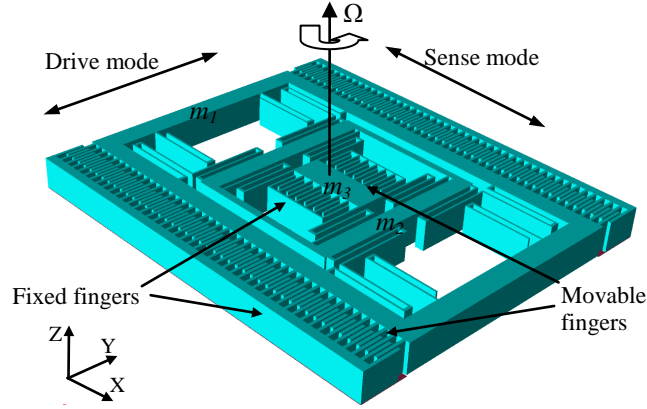
Figure 5.1. Prototype of the 4-DOF gyroscope.

Similar to the 4-DOF non-resonant gyroscope design concept reported in [22, 23], the gyroscope in this chapter contains three proof masses that are linked together with several well-arranged folded-beams. The beam design allows m_1 to move only in the drive-mode direction; m_2 and m_3 can only move together in this direction. Therefore, m_1 and the combination of m_2 and m_3 form a 2-DOF drive oscillator. For the sense-mode direction, m_2 and m_3 are movable to each other and they form a 2-DOF sense oscillator. The 4-DOF gyroscope can therefore be lumped into two oscillator models as shown in Figure 5.2.

(a)   (b)
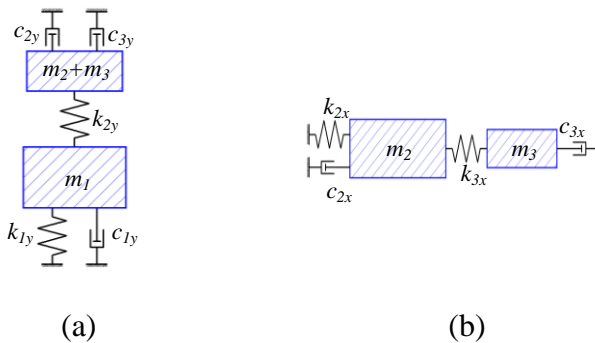
Figure 5.2. Lumped models of the 4-DOF non-resonant gyroscope: (a) drive mode and (b) sense mode.
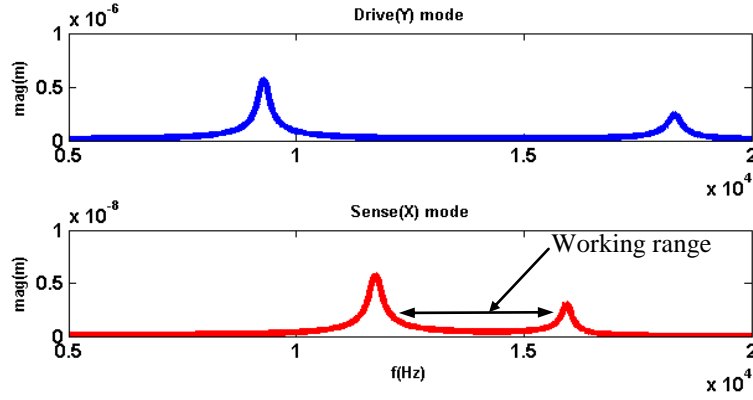
Figure 5.3. Working range of the gyroscope.

The steady-state frequency response of the gyroscope has two resonance peaks and a relatively flat region in between (Figure 5.3). The gyroscope is less vulnerable to the shift of resonant frequencies when it operates in the flat region. In order to achieve high robustness, the non-resonant gyroscope is designed to work in the overlapped flat regions of the drive and sense modes. Compared to the conventional resonant gyroscope, the non-resonant gyroscope has a wide working range and it is less vulnerable to the fabrication uncertainties.

5.2 Device performance simulation

To obtain a better understanding of the device's characteristics, we use the behavior model approach module in CoventorWare. This approach provides quick frequency response of the device under different mechanical and electrical configurations. Solutions can be obtained within a few seconds with good accuracy. The corresponding 3D model of the 4-DOF non-resonant gyroscope is created by CoventorWare and the layout is shown in Figure 5.4.
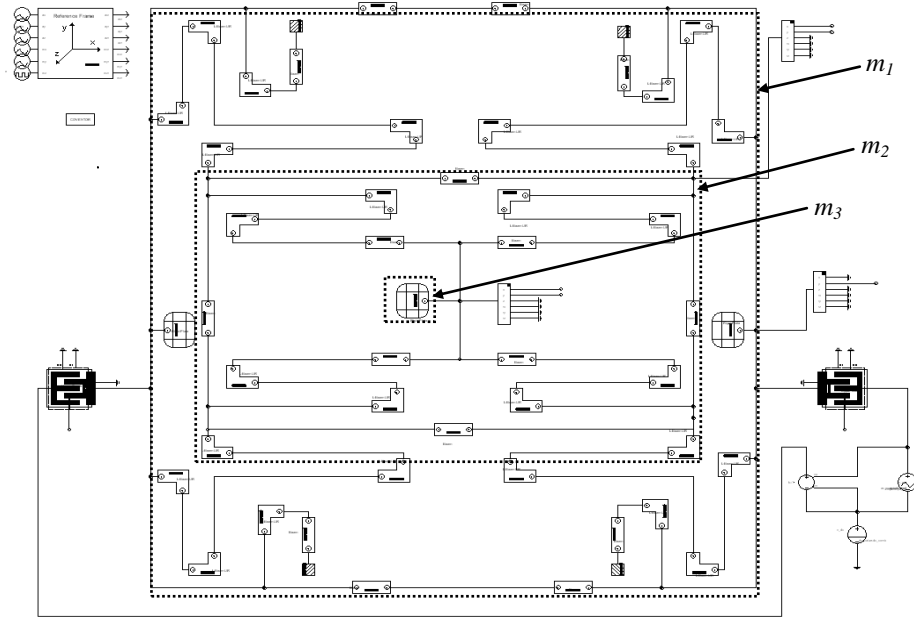
Figure 5.4. Schematic layout of the non-resonant gyroscope.

The schematic layout is composed of various components, which are used to model the mechanical and electronic behaviors of the gyroscope. The components include beams, L-beams, anchors, rigid plates, fixed fingers, bus connectors, reference frames and signal sources as listed in Table 5.1.

Table 5.1. Components used in the schematic layout of the non-resonant gyroscope.

	Beam		Fixed fingers
	L-beam		Bus connector
	Anchor		Reference frame
	Rigid plate and movable fingers		Alternating voltage

The reference frame is used to apply accelerations and angular velocities relative to the reference coordinate system. The angular velocity of the gyroscope is set up as 10 rad/s. The bus connectors are used to probe DOF or to apply boundary conditions at the individual DOF [34], e.g. to apply damping to a proof mass.

5.2.1 Damping extraction

Unless the MEMS device operates in a vacuum environment, the viscous damping has to be considered. Due to the small dimensions of the device, the effect of viscous damping is orders of magnitude higher than that of the damping of structural material. In general, the viscous damping can be divided into two categories. One type is slide-film damping where the plates move along each other (Figure 5.5 (a)); the other type is squeeze-film damping where two plates move towards each other (Figure 5.5 (b)).

(a)   (b)

Figure 5.5. 3D illustrations of (a) slide-film damping and (b) squeeze-film damping.

When a plate moves along or perpendicular to its surface with a small oscillation of frequency, the air in the gap applies a force to the plate and $F = \dot{c}x + kx$. The force has two components; $\dot{c}x$ is the damping force and kx is the spring force. Both forces are frequency-dependent and air pressure-dependent. The damping coefficient is the ratio of the damping force to the amplitude of the velocity of the mass. At the low frequency range, the slide-film damping coefficient can be expressed by [51]:

$$c_{slide} = \mu A / g \qquad (5.1)$$

where μ is the viscosity constant for air and $\mu = 1.84 \times 10^{-5}$ kg/s at 27°C, A is the area of the plate, and g is the gap between the plates.

When the gyroscope system is in motion, the slide-film damping occurs at two regions: one is the gap between the gyroscope and the silicon substrate; the other is between the movable fingers and the fixed fingers. The squeeze-film damping occurs when the gyroscope squeezes the air between the movable and fixed fingers. Using Blech's model [52], the slide-film damping coefficient can be estimated as:

$$c_{slide}(\omega) = \frac{768}{\pi^4} \frac{a^3 b}{g^3} \mu \sum \frac{m^2 + n^2 (a/b)^2}{m^2 n^2 [m^2 + n^2 (a/b)^2]^2 + \sigma^2 / \pi^4} \qquad (5.2)$$

where a is the plate width, b is the plate length, and σ is the squeeze number:

$$\sigma = 12 \left(\frac{a}{g} \right)^2 \left(\frac{\omega}{P} \right) \qquad (5.3)$$

where ω is the frequency of the motion and P is the air pressure.

When the squeeze number σ is much smaller than π^2, in other words, ω / P is small, Eqn. (5.2) is reduced to a constant [53]:

$$c_{squeeze} = 0.42(A)^2 \mu / g^3 \qquad (5.4)$$

For the same set of comb fingers, both types of damping may occur alternatively with respect to the motion of the movable fingers as illustrated in Figure 5.6.
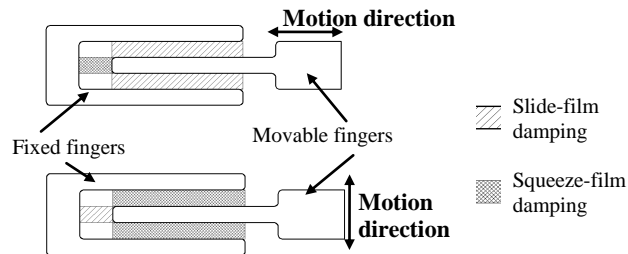
Figure 5.6. Damping distribution for a comb drive.

The damping applied to each proof mass is calculated and the corresponding macromodels are created in CoventorWare. By taking the viscous damping effects into consideration, the model of the gyroscope becomes more accurate.

Both the slide-film damping and the squeeze-film damping occur when m_1 is oscillating in the drive-mode direction. Figure 5.7 shows the simulation result of the damping coefficient plotted against the frequency.
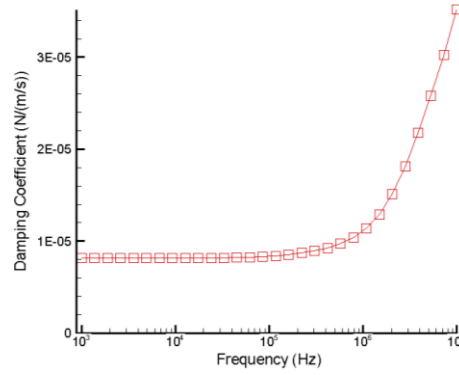
Figure 5.7. Damping coefficient c_{1y}.

At the low frequency range, the damping coefficient c_{1y} can be estimated approximately as 8.55×10^{-6} N/(m/s). Combining Eqn. (5.1) and Eqn. (5.4), the analytical estimation of the damping is 8.43×10^{-6} N/(m/s). The damping coefficient shows a sharp increase at the high frequency range.
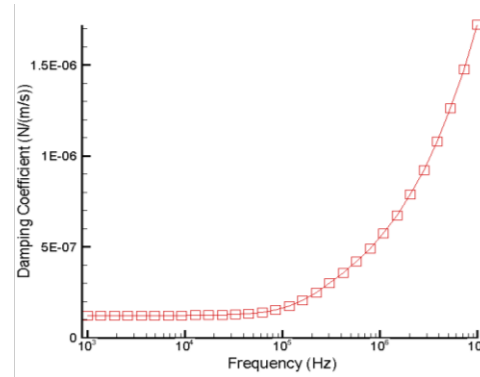
Figure 5.8. Damping coefficient $c_{2y} = c_{2x}$.

When m_2 is in motion, only the slide-film damping between the gyroscope system and the silicon substrate is applied to the proof mass. The effect of damping is independent to the moving direction of m$_2$. Hence, the damping coefficient c_{2y} is the same as c_{2x}. Figure 5.8 shows the trend of the damping coefficient as a function of frequency. At the low frequency range, c_{2y} and c_{2x} is a constant as approximately 1.25×10^{-7} N/(m/s). The value is close to the estimation of 1.24×10^{-7} N/(m/s) given by Eqn. (5.1).

Similarly, when m_3 oscillates in the drive mode, only the slide-film damping is applied to the proof mass. The simulation result of c_{3y} is obtained as 4.98×10^{-7} N/(m/s) at the low frequency range. The value is close to the analytical estimation of 5.02×10^{-7} N/(m/s). The damping coefficient c_{3y} increases at the high frequency range (Figure 5.9).
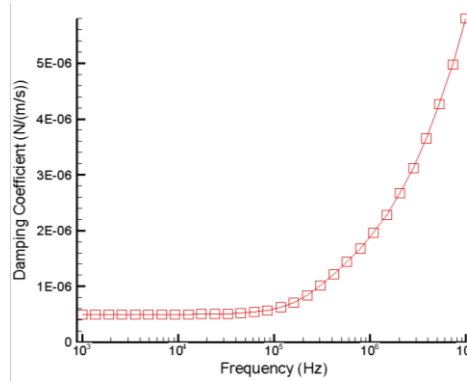
Figure 5.9. Damping coefficient c_{3y}.
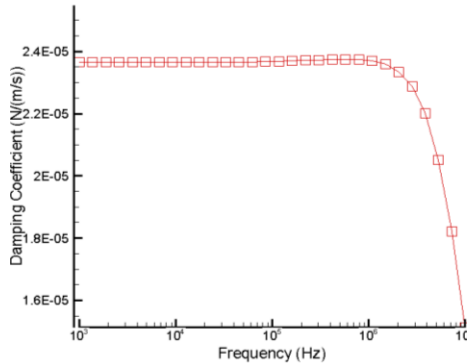
Figure 5.10. Damping coefficient c_{3x}.

When m_3 oscillates in the sense mode, the squeeze-film damping occurs between the movable and fixed fingers. Figure 5.10 shows c_{3x} plotted against the frequency of the motion. In the low frequency range, c_{3x} remains constant. It shows a sharp decrease after the frequency reaches 10^6 Hz. This figure shows a typical trend of squeeze-film damping. In the high frequency range, the air is squeezed and expelled out of the gap between the fingers, and this causes the pressure and viscosity to decrease. Therefore, the squeeze-film damping coefficient is reduced. Table 5.2 summarizes the simulation results of the damping coefficient in the low frequency range and their analytical counterparts.

Table 5.2. Damping coefficient N/(m/s) obtained by the analytical equations and simulation.

	Analytical	Simulation	Change
c_{1y}	8.43×10^{-6}	8.55×10^{-6}	1.40%
c_{2x}	1.24×10^{-7}	1.25×10^{-7}	0.80%
c_{2y}	1.24×10^{-7}	1.25×10^{-7}	0.80%
c_{3x}	1.89×10^{-5}	2.36×10^{-5}	19.9%
c_{3y}	5.02×10^{-7}	4.98×10^{-7}	-0.80%

The analytical and simulation results show close matches except the damping coefficient c_{3x} for which the simulated value is 19.9% higher. The mismatch can be explained by the assumptions described by J. Blech [52]: the pressure on the edges jump to the ambient pressure (an ideal edge condition). The simulation results from CoventorWare account for non-ideality of the edges and are therefore bigger than the analytical estimation [34].

The damping macromodels are created after the damping simulation. They are attached to the bus connectors as shown in Figure 5.11. The damping components are connected to the corresponding DOFs. For instance, c_{1y} occurs when m_1 oscillates along the drive-mode direction, therefore the macromodel is connected to the y-pin of the bus connector. It represents that the damping is applied to the translational DOF in Y-axis. All other pins (x, z, rx, ry, rz) of the bus connector are grounded because the motions are not of our interests.
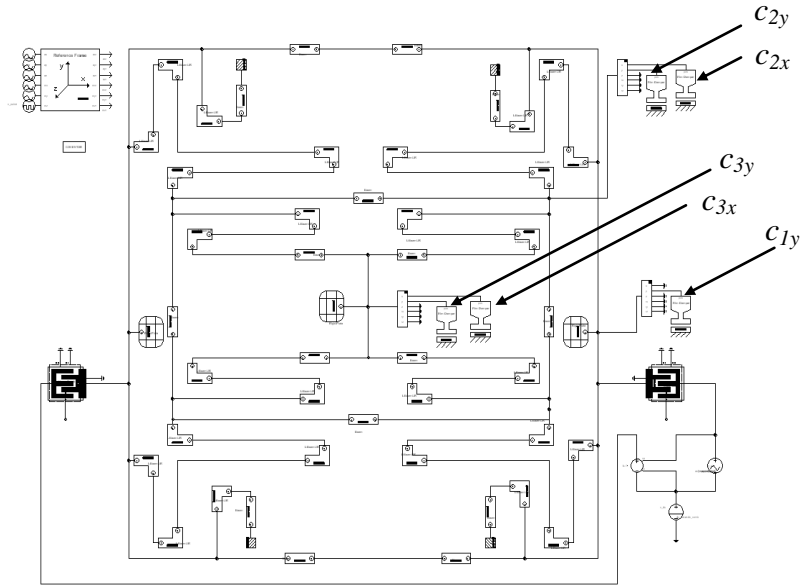
Figure 5.11. The schematic layout of the non-resonant gyroscope with damping macromodels.

5.2.2 Frequency response analysis

The frequency response analysis is conducted based on the schematic layout. The total simulation time is less than ten seconds with comparable accuracy to that obtained

by traditional FEM. The angular velocity is set as 10 rad/s. Figure 5.12 shows the frequency response.
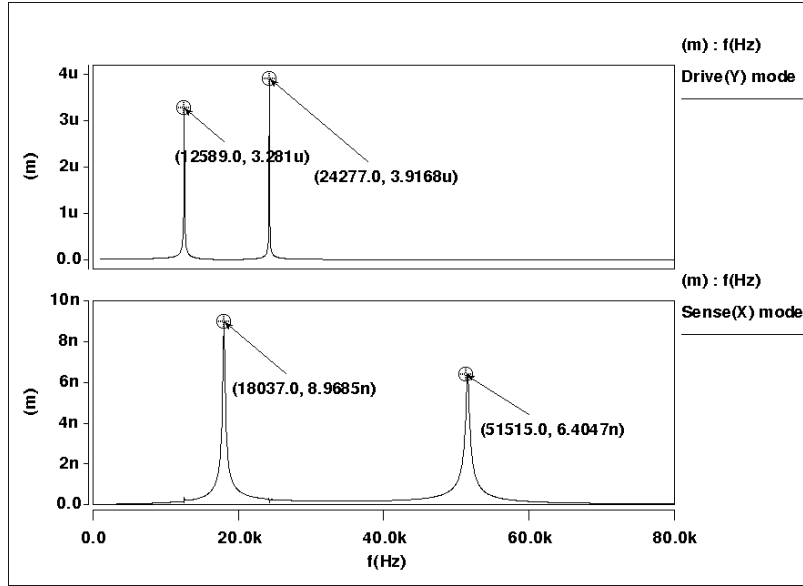
Figure 5.12. Original frequency response: (top trace) drive mode and (bottom trace) sense mode.

The results indicate that the flat regions of the drive and sense modes are not well overlapped. Based on the operation principle of the 4-DOF non-resonant gyroscope, the working range of the device is narrow and optimization is therefore needed.

5.2.3 Design optimization

To achieve both high robustness and wide working range, the gyroscope needs to be optimized to increase the overlapped region of the drive and sense modes. Because the frequency is a function of the stiffness, we sweep three spring constants k_{1y}, k_{2y}, and k_{3x} to obtain desirable frequency response. The gyroscope is symmetric along X and Y axes, with each spring constant defined by four folded-beams. The spring constants and their corresponding beams in one-fourth of the gyroscope are labeled in Figure 5.13.

71
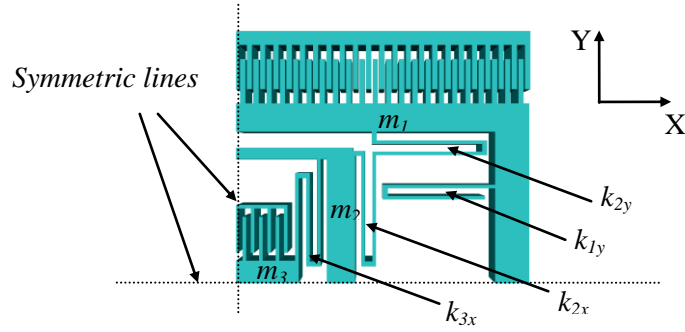
Figure 5.13. Spring constants in one-fourth of the gyroscope.

Our first attempt is to adjust k_{1y}. Because spring constant depends on the dimensions of beams, we adjust k_{1y} by changing the width of the beams. Figure 5.14 shows the frequency response with various beam widths. The width is changed from 4 to 16 μm with an increment of 4 μm.
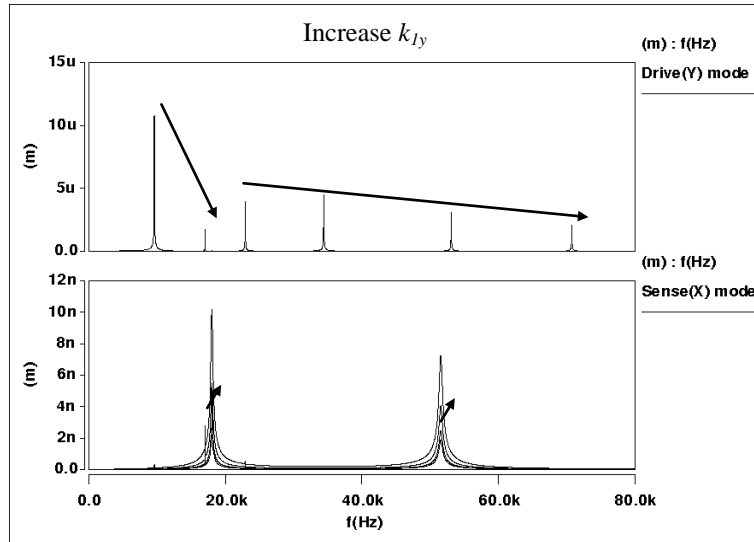
Figure 5.14. Effect of k_{1y} on the resonant frequencies.

Both resonant frequencies of the drive mode shift to the right when the width increases. However, the peak of the first resonant frequency is indiscernible when the width is over 8 μm. The overlapped flat region of the drive and sense modes has a trade-

off with the high amplitude of the resonant frequency. As a result, the compromised width is chosen as 8 μm.
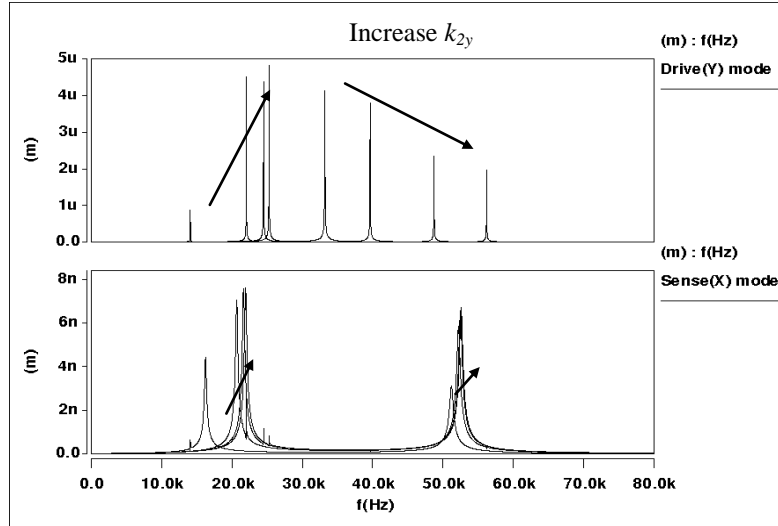
Figure 5.15. Effect of k_{2y} on the resonant frequencies.

The same optimization approach is conducted on k_{2y}. The width of the beams is adjusted from 4 to 16 μm with a 4 μm increment. Figure 5.15 shows the effect of k_{2y} on the resonant frequencies. The frequency response demonstrates that the effect of k_{2y} is negligible on the sense mode. The flat region is well overlapped with the flat region of the drive mode when the width of the beams is 12 μm.

However, the amplitude of the flat region is only a few hundred pm (picometers, 10^{-15} m). Because of the tradeoff between the bandwidth and the amplitude of frequency, we shrink the flat region to improve the amplitude.
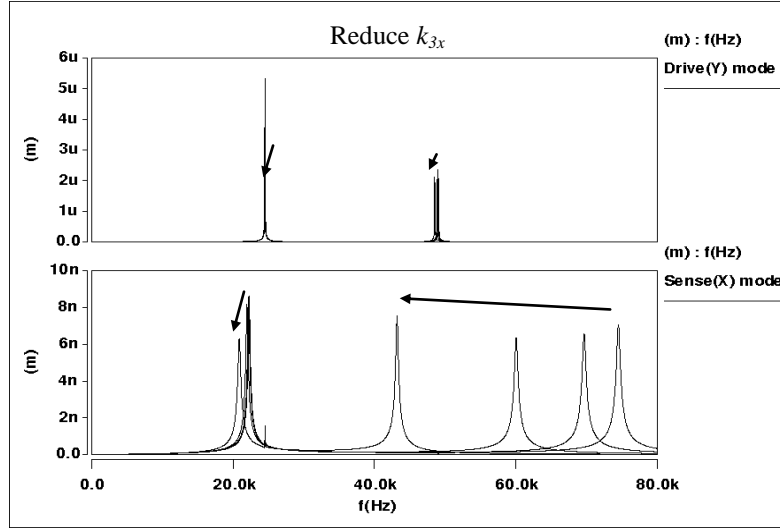
Figure 5.16. Effect of k_{3x} on the resonant frequencies.

Figure 5.16 shows the reduction of the flat region when k_{3x} is reduced. The width of the beam is decreased from 10 to 4 μm with a decrement of 2 μm. As shown in the figure, a smaller width leads to a narrower flat region. Nevertheless, 4-μm features often require extra constraints, which increase the cost of the fabrication process. The width is therefore selected as 6 μm.
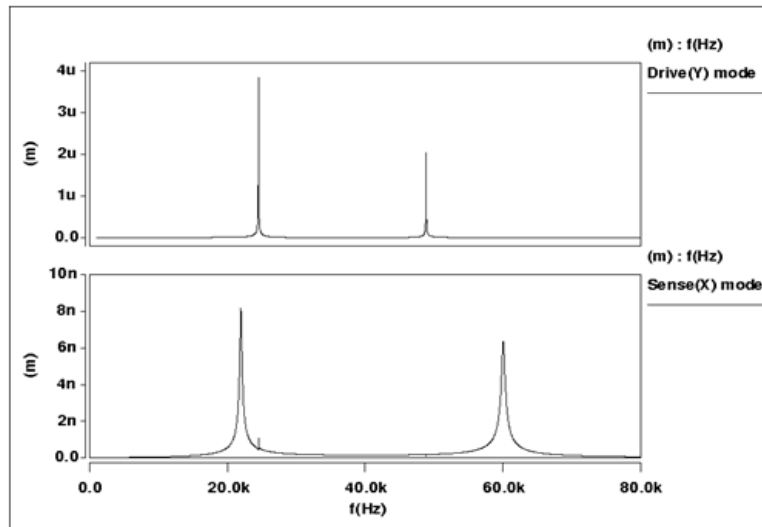
Figure 5.17. Frequency response of the optimized gyroscope.

Figure 5.17 shows the frequency response of the optimized gyroscope. The optimized gyroscope has a wide overlapped region of the drive and sense modes. However, the peaks of the resonant frequencies of the sense mode lead to large amplitude change which may cause sensitivity uncertainties and the fatigure problem. Therefore, large damping is induced to reduce the amplitude while keeping the overlapped region relatively constant.

The large damping can be achieved by decreasing the gaps of the comb fingers. The gaps between the comb fingers are adjusted from 2.8 to 1.9 μm with a decrement of 0.3 μm. As a result, the damping coefficient c_{3x} is increased from 5.69×10^{-4} to 1.82×10^{-3} N/(m/s).
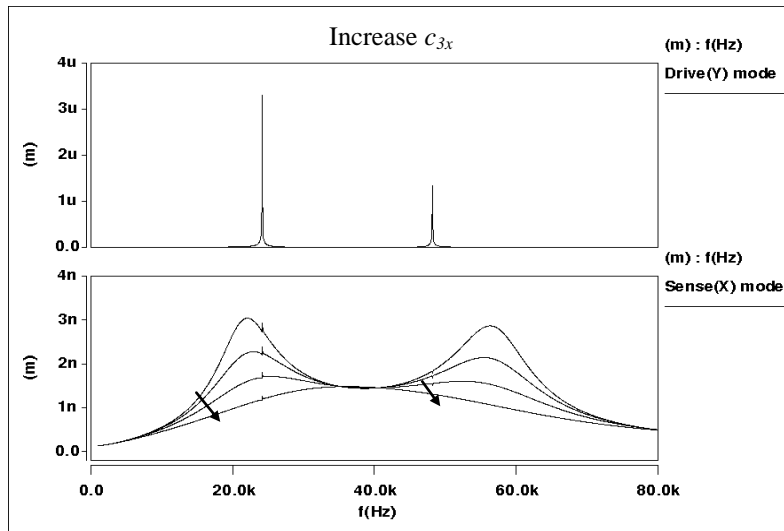
Figure 5.18. Effect of c_{3x} on the sense mode.

As illustrated in Figure 5.18, the range of the flat region is not much affected by the drastic change in the damping coefficient. This shows that the fabrication uncertainties induced damping shift has little effect on the working range. The optimum damping coefficient is determined as 1.17×10^{-3} N/(m/s) with a gap of 2.2 μm. At this condition, the sense mode frequency response shows a wide flat region (Figure 5.19).

75
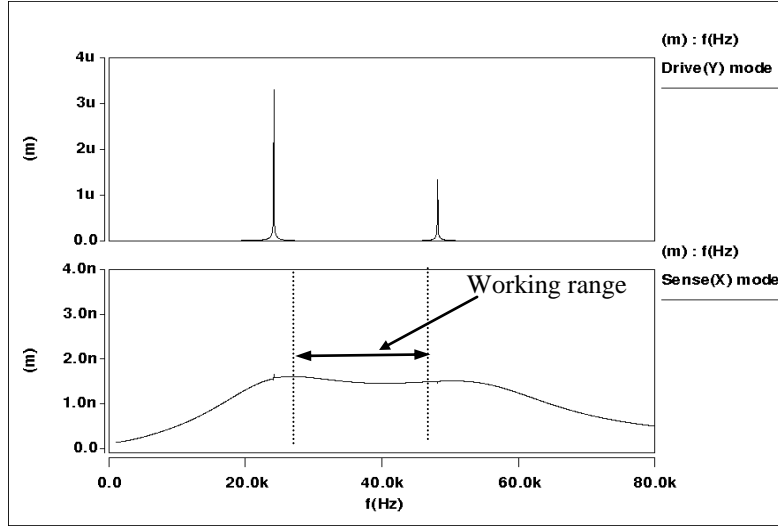
Figure 5.19. Optimized frequency response of the non-resonant gyroscope with proper damping.

The induced damping raises the amplitude of the sense mode frequency response to a nearly constant value. However, the frequency response amplitude is small. As the angular velocity is raised from 10 to 100 rad/s, the amplitude of the flat region is only raised from a few hundred pm to a few nm. Further investigation is needed to improve the amplitude of the frequency. In this chapter, all the design parameters are optimized individually. The optimum condition may require a thorough study of coupling of different parameters.

5.3 Discussions and conclusions

This chapter investigates a 4-DOF non-resonant gyroscope using behavior model analysis in CoventorWare. The damping is analyzed and extracted as behavior macromodels. The damping coefficient is verified by analytical slide-film and squeeze-film models. The design is optimized by spring constant sweeping to increase the overlapped region of the drive and sense modes. By decreasing the gaps between the

comb fingers to increase the damping, the response of the sense mode is adjusted to have a wide and flat working frequency range. The investigation and optimization presented in this chapter demonstrate that the 4-DOF non-resonant gyroscope is an effective device to overcome resonant frequency shift caused by fabrication uncertainties.

FEEDBACK CONTROL OF A NON-RESONANT MEMS GYROSCOPE

Compared to conventional MEMS gyroscopes, non-resonant gyroscopes are less vulnerable to fabrication perturbations. However, our simulation results show that under ±10% parameter variations, the scale factor error is over 10% over the robust operation range (the flat region between two resonant peaks) and the closed-loop performance of non-resonant gyroscopes has not been investigated previously. In this chapter, we investigate the control of a non-resonant MEMS gyroscope with the linear quadratic regulator (LQR) to improve the scale factor error under fabrication imperfections. The compensators are designed in MATLAB and the device performance is analyzed using behavior models in CoventorWare with the embedded controllers. The performance of the closed-loop non-resonant gyroscope and the scale factor error under parameter variations are analyzed and reported in this chapter.

6.1 Transfer function

The 4-DOF non-resonant gyroscope design used in this chapter is same as the one in the last chapter. Figure 5.1 illustrates the 3D model of the gyroscope. The 4-DOF gyroscope can be modeled as two mass-damper-spring models as shown in Fig. 6.1.
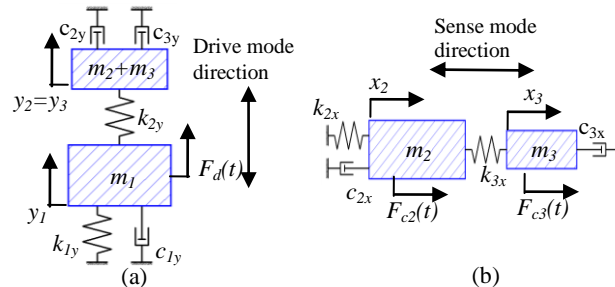
Figure 6.1. Lumped models of the 4-DOF non-resonant gyroscope: (a) drive mode and

(b) sense mode.

From Figure 6.1, the system governing equations are expressed by

Drive-mode direction:

$$\begin{cases} m_1\ddot{y}_1 + c_{1y}\dot{y}_1 + k_{1y}y_1 = k_{2y}(y_2 - y_1) + F_d(t) \\ (m_2 + m_3)\ddot{y}_2 + c_{2y}\dot{y}_2 + k_{2y}y_2 = k_{2y}y_1 \end{cases} \tag{6.1}$$

Sense-mode direction:

$$\begin{cases} m_2\ddot{x}_2 + c_{2x}\dot{x}_2 + k_{2x}x_2 = k_{3x}(x_3 - x_2) + F_{c2}(t) \\ m_3\ddot{x}_3 + c_{3x}\dot{x}_3 + k_{3x}x_3 = k_{3x}x_2 + F_{c3}(t) \end{cases} \tag{6.2}$$

where m, c, and k stand for mass, damping coefficient, and spring constant, respectively.

$F_d(t)$ is sinusoidal excitation force. $F_{c2}(t) = 2m_2\Omega_z\dot{y}_2$ and $F_{c3}(t) = 2m_3\Omega_z\dot{y}_2$ are rotation-

induced Coriolis forces. m_1 of the 2-DOF drive mode oscillator is driven into resonance

by $F_d(t)$. The main design objective in the drive mode is to maximize the Coriolis force

generated by m_2, which is the dominant force leading to the sense-direction oscillation.

For the 2-DOF sense-direction oscillator, the design objective is to maximize x_3, which is

the sense direction oscillation amplitude of the sensing element m_3. In non-resonant

gyroscope designs, m_3 is usually much smaller than m_2. Therefore, the transfer function

of the sense mode (the ratio of the response of m_3 to the angular rate input) can be

simplified as:

$$G(s) = \frac{k_{3x}m_2}{m_2m_3s^4 + (c_{2x}m_3 + m_2c_{3x})s^3 + (k_{2x}m_3 + k_{3x}m_3 + c_{2x}c_{3x} + m_2k_{3x})s^2 + }$$

$$\overline{(k_{2x}c_{3x} + k_{3x}c_{3x} + c_{2x}k_{3x})s + k_{2x}k_{3x}} \tag{6.3}$$

Dynamic systems with two coupled proof masses have two resonance peaks. The amplitude of the flat region between the two resonance peaks is less vulnerable to the resonant frequency shift when the gyroscope operates in the flat region. Therefore, to achieve high robustness, the non-resonant gyroscope is designed to operate in the overlapped flat regions of the drive and sense modes (Fig. 6.2).
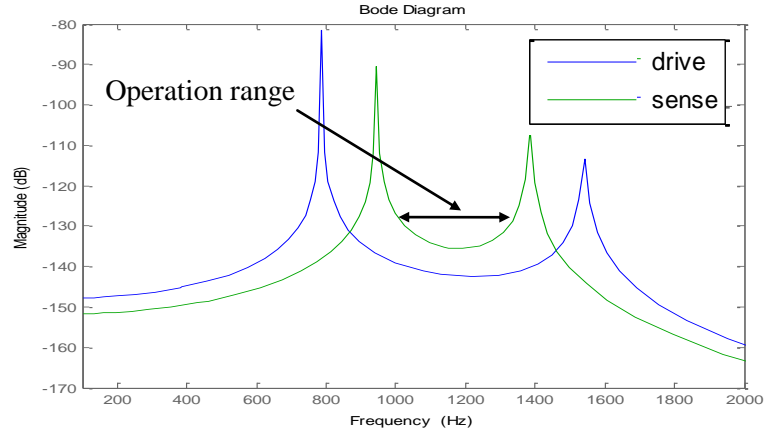
Figure 6.2. Designed operation range of the non-resonant gyroscope.

Despite its inherent robustness, an open-loop non-resonant gyroscope has limited performance in terms of narrow bandwidth and sluggish system response. In this study, we focus on the controller design of the sense mode response of m_3. The drive loop can also be controlled using different control methods such as automatic gain control (AGC) [48]. To reduce the design complexity, we assume the amplitude of the drive mode motion is well monitored and sustained, i.e., the amplitude of the drive mode oscillation is well sustained under parameter variations.

6.2 Compensator design

A compensator in state-space consists of a controller and an estimator. The controller defines the control law for the closed-loop system while the estimator is used to reconstruct all the state variables of a system. If all state variables are measurable and available for feedback, the estimator is not required. In reality, however, only the system output is available for feedback. Therefore, the reconstructed state variables by the estimator are needed for the compensator design.

One of the most effective and widely used techniques of linear control systems design is the LQR method. Figure 6.3 shows the block diagram of the LQR closed-loop system. The state-space representation for the sense mode non-resonant gyroscope is given by:

Plant:

$$\begin{cases} \dot{\mathbf{x}} = \mathbf{F}\mathbf{x} + \mathbf{G}u \\ y = \mathbf{H}\mathbf{x} \end{cases} \tag{6.4}$$

Compensator:

$$\begin{cases} \dot{\hat{\mathbf{x}}} = \mathbf{F}\hat{\mathbf{x}} + \mathbf{G}u + \mathbf{L}(y - \mathbf{H}\hat{\mathbf{x}}) \\ u = -\mathbf{K}\hat{\mathbf{x}} + \overline{N}r \end{cases} \tag{6.5}$$

where $\overline{N}$ is the gain factor on the reference input, $\mathbf{x} = [x_2, \dot{x}_2, x_3, \dot{x}_3]^{\mathrm{T}}$ is all the states, $\hat{\mathbf{x}}$ is an estimate state of $\mathbf{x}$, $\mathbf{K} = [K_1, K_2, K_3, K_4]$ is the controller gain, $\mathbf{L} = [L_1, L_2, L_3, L_4]^{\mathrm{T}}$ is the estimator gain, the system matrix,

$$\mathbf{F} = \begin{bmatrix} 0 & 1 & 0 & 0 \\ -\dfrac{(k_2 + k_3)}{m_2} & -\dfrac{c_2}{m_2} & \dfrac{k_3}{m_2} & 0 \\ 0 & 0 & 0 & 1 \\ \dfrac{k_3}{m_3} & 0 & -\dfrac{k_3}{m_3} & -\dfrac{c_3}{m_3} \end{bmatrix}, \text{ the input matrix } \mathbf{G} = \begin{bmatrix} 0 & 1 & 0 & 0 \end{bmatrix}^{\mathrm{T}}, \text{ and the}$$

output matrix $\mathbf{H} = \begin{bmatrix} 0 & 0 & 1 & 0 \end{bmatrix}$.
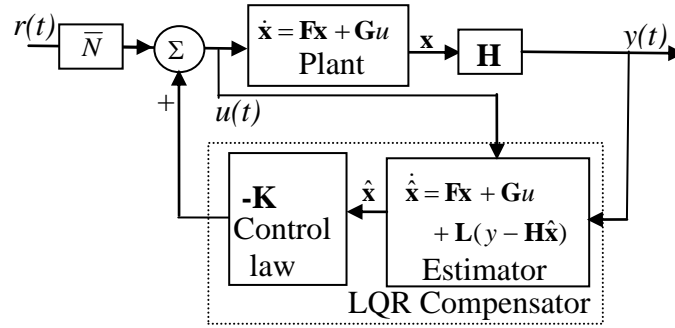
Figure 6.3. Block diagram of state-space design elements.

The overall closed-loop system equations in the standard form are:

$$\begin{cases} \dot{\mathbf{x}}_{\mathrm{cl}} = \mathbf{A}_{\mathrm{cl}} \mathbf{x}_{\mathrm{cl}} + \mathbf{B}_{\mathrm{cl}} r \\ y = \mathbf{C}_{\mathrm{cl}} \mathbf{x}_{\mathrm{cl}} + \mathbf{D}_{\mathrm{cl}} r \end{cases} \tag{6.6}$$

where the system matrices are $\mathbf{A}_{\mathrm{cl}} = \begin{bmatrix} \mathbf{F} & -\mathbf{GK} \\ \mathbf{LH} & \mathbf{F} - \mathbf{GK} - \mathbf{LH} \end{bmatrix}$, $\mathbf{B}_{\mathrm{cl}} = \begin{bmatrix} \overline{N}\mathbf{G} & \mathbf{0} \end{bmatrix}^{\mathrm{T}}$,

$\mathbf{C}_{\mathrm{cl}} = \begin{bmatrix} \mathbf{H} & \mathbf{0} \end{bmatrix}$, $\mathbf{D}_{\mathrm{cl}} = [0]$, and $\mathbf{x}_{\mathrm{cl}} = \begin{bmatrix} \mathbf{x} & \hat{\mathbf{x}} \end{bmatrix}^{\mathrm{T}}$. The optimal values of $\mathbf{K}$ and $\mathbf{L}$ are those

which place the closed-loop poles at the stable roots of the symmetric root locus (SRL)

equation:

$$1 + \rho G(s)G(-s) = 0 \tag{6.7}$$

where ρ is a weighing factor of the designer's choice, $G(s)$ is the open-loop transfer

function (Eqn. (6.3)). Choosing different values of ρ can provide us with different pole

locations that achieve different tradeoff between a fast response and a low control effort.

With the selected controller and estimator poles, we can then compute the controller gain ($\mathbf{K}$) and the estimator gain ($\mathbf{L}$) by Ackermann's formula and the compensator transfer function as follows:

$$D_c(s) = -\mathbf{K}(s\mathbf{I} - \mathbf{F} + \mathbf{GK} + \mathbf{LH})^{-1}\mathbf{L} \tag{6.8}$$

Based on Fig. 6.3, the closed-loop transfer function ($CLTF$) is:

$$CLTF = \frac{G(s)}{1 + D_c(s)G(s)} \tag{6.9}$$

Inserting Eqn. (6.3) and Eqn. (6.8) into Eqn. (6.9), the closed-loop DC gain becomes:

$$\left.|CLTF|\right|_{s \to 0} = \frac{m_2}{k_{2x} + m_2 K} \tag{6.10}$$

where K is the compensator gain which can be determined from Eqn. (6.8) with s = 0. Uniform scale factor is necessary for reliable performance of MEMS gyroscopes. If the same fabrication tolerance is assumed for all the parameters, beam width variation which leads to spring constant change has the highest effect on the system frequency response [54]. Because 20% (±10%) perturbation ratio is the common manufacturing error ratio of MEMS inertial sensors [43], ±10% spring constant variations are applied to the MEMS gyroscope in this study. The scale factor uniformity error under the fabrication perturbations can be defined as:

$$\Delta S = \frac{A_{max} - A_{min}}{A_{max}} \tag{6.11}$$

where A is the DC gain of the gyroscope. A_{max} and A_{min} correspond to the maximum and the minimum DC gains under ±10% spring constant variations. For the open-loop system, $A = \left.|G(s)|\right|_{s \to 0} = m_2 / k_{2x}$; for the closed-loop system, $A = \left.|CLTF|\right|_{s \to 0}$. Therefore, k_{2x} has an effect on the DC gain A and the scale factor error ΔS under fabrication uncertainties.

Previously, researchers have reported closed-loop resonant gyroscopes with scale factor errors less than 1% [43, 48]. In this work, we are targeting a scale factor error of 1% as our design specification. The compensator uses the design data (proof mass, spring constant) of an SOI MEMS gyroscope developed by the University of California, Irvine [51]. The damping coefficients are determined from the analytical slide-film and squeeze-film models [49]. The parameters of the gyroscope are listed in Tab. 6.1. Under $\pm10\%$ k_{2x} variations, the scale factor criterion $\Delta S = 1\%$ with respect to the compensator gain K becomes:

$$K = 18.9 \frac{k_{2x}}{m_2} = 3.54 \times 10^9 \qquad (6.12)$$

Table 6.1. Design parameters of the non-resonant gyroscope.

Parameters	Value	*Parameters*	Value
m_2 *(kg)*	7.67×10^{-7}	m_3 *(kg)*	7.29×10^{-8}
c_{2x} *(N/m/s)*	2×10^{-7}	c_{3x} *(N/m/s)*	3×10^{-5}
k_{2x} *(N/m)*	144	k_{3x} *(N/m)*	13.6

Figure 6.4 plot the symmetric root locus of the gyroscope. The solid lines are the paths of all possible closed-loop poles which include the controller poles and estimator poles. Four diamond-shaped markers indicate the controller pole locations (-4.70±2.28i and -1.93±5.46i kHz) that meet $\Delta S = 1\%$ with a corresponding compensator gain K of 3.54×10^9. The estimator poles are selected to be (-37.60 ±18.24i and -15.44±43.68i kHz) eight times faster than the controller poles in order to reduce the influence of the estimator poles on the entire system. Figure 6.5 shows the closed-loop step response with a settling time of 0.5 ms. The closed-loop DC gain is approximately 2.68×10^{-10} which

meets the analytical estimation of $\dfrac{m_2}{k_{2x} + m_2 K} = 2.68 \times 10^{-10}$. Based on Eqn. (6.10) and

(6.11), we have $\Delta S = \dfrac{A_{\max} - A_{\min}}{A_{\max}} = 1 - \dfrac{k_{2x\min} + m_2 K}{k_{2x\max} + m_2 K}$, which suggests that a smaller $\varDelta S$

requires a larger compensator gain K. Therefore, the high robustness of the LQR

compensator is achieved at the cost of an increased compensator gain K.
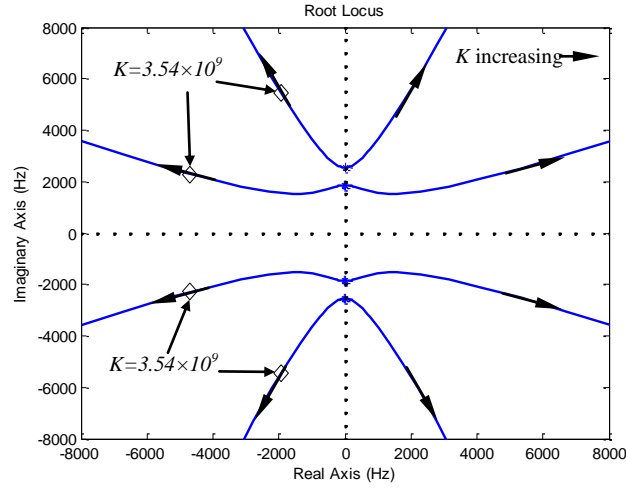
Figure 6.4. Symmetric root locus of the non-resonant gyroscope.
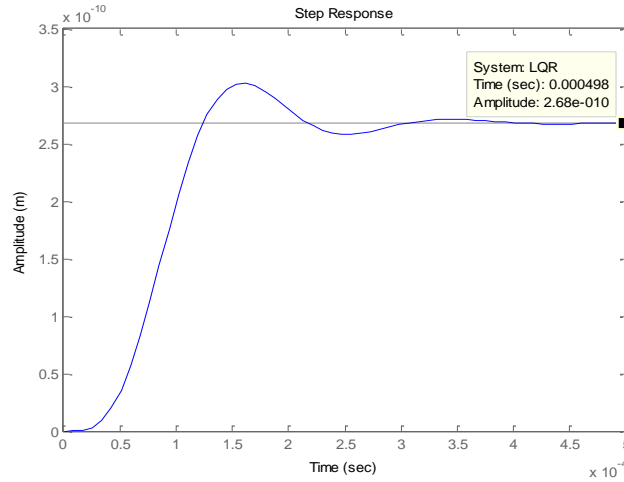
Figure 6.5. Closed-loop step response of the SRL design.

6.3 Robustness analysis

In this section, we test our designs and compare the robustness of the open-loop and the closed-loop gyroscopes under ±10% k_{2x} variations in CoventorWare. The LQR compensator gain K is 3.54×10^9 to achieve the scale factor criterion. Figure 6.6 shows the responses of the three cases under the step input. The top trace is the step input Coriolis acceleration with an amplitude of 1 m/s^2. The second trace is the open-loop response. The settling time of the system is approximately 30 ms. The nominal open-loop output is 5.32 nm. +10% and -10% perturbation ratios lead to the steady-state values of 4.83 nm and 5.92 nm, respectively. According to the definition, the scale factor error can be calculated as $\Delta S = \dfrac{5.92 \times 10^{-9} - 4.83 \times 10^{-9}}{5.92 \times 10^{-9}} = 18.41\%$. The bottom trace is the LQR control system response. The LQR design has shorter settling time than the system without the control loop. The nominal output is 268.9 pm. The perturbation results in a 1% error, which matches the analytical estimation of $1 - \dfrac{k_{2x\min} + m_2 K}{k_{2x\max} + m_2 K} = 1\%$ given by Eqn. (6.11).

Figure 6.6. Simultion results of the non-resonant gyroscope under k_{2x} variations:

86

(top trace) angular rate input, (middle trace) open-loop step response, and (bottom trace) closed-loop response.

Step response is equivalent to the response of the system operating at a very low frequency. Because the non-resonant gyroscope usually operates in the flat region between the two resonance peaks, the robustness of the compensator under the operational frequency is investigated next. The open-loop frequency response under $\pm 10\%$ variations of k_{2x} is shown in Fig. 6.7(a). The flat region between the two resonance peaks is approximately 2 kHz through 2.4 kHz. Therefore, the working range is approximately 400 Hz. The solid line is the nominal response. The dotted line and the dashed line are the responses under +10% and -10% k_{2x} variations, respectively. The minimum amplitude within the flat region is 56.41 nm and 50.91 nm under $\pm 10\%$ k_{2x} variations. Therefore, according to Eqn. (6.11), the variations result in approximately 10% scale factor error. Figure 6.7(b) is the frequency response of the LQR control system under $\pm 10\%$ k_{2x} variations. Same types of lines are used to illustrate the responses in terms of different k_{2x}. The closed-loop working range is increased to 5.88 kHz and the system is robust over a wide frequency range. Under $\pm 10\%$ k_{2x} variations, A_{max}-A_{min} is less than 5 pm over 2.5 kHz. At the operational frequency of 2.2 kHz, +10% and -10% perturbation ratios lead to the amplitudes of 268.76 pm and 268.81 pm, respectively. Therefore, the scale factor error is approximately 0.018%.
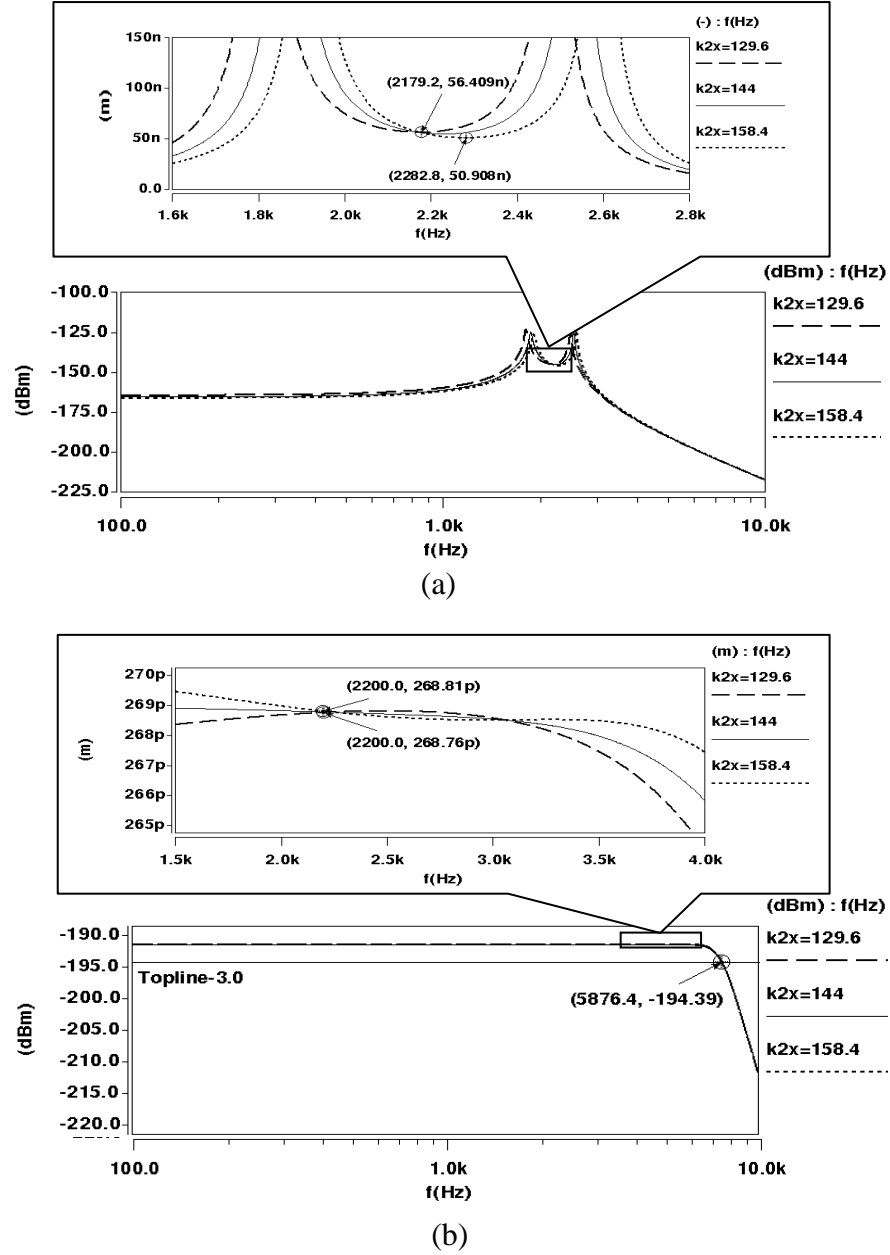
Figure 6.7. Effect of k_{2x} variations on the (a) open-loop response and (b) the LQR

controlled response.

To accurately measure the scale factor error, Figure 6.8 plots the transient

responses to the sinusoidal input angular rate at the operational frequency (2.2 kHz)

under $\pm 10\%$ k_{2x} variations. The Coriolis acceleration input with an amplitude of 1 m/s^2 is

depicted in the top trace. The second trace is the uncontrolled response which has the stabilized peak-to-peak error of 6.49 nm. The simulation shows that the maximum output is 58.69 nm. Therefore, the scale factor error is 11.06%, which matches the result in the frequency response analysis in Fig. 6.7(a). The third trace is the LQR controlled response with the maximum amplitude of 268.64 pm. The stabilized peak-to-peak error is 38.33 fm under the parameter variations. The resulting scale factor error is 0.014%, which is close to the result in the frequency response analysis in Fig. 6.7(b). The LQR compensator shows outstanding performance compared to the controller designs for the resonant gyroscopes reported in other research [43, 48].
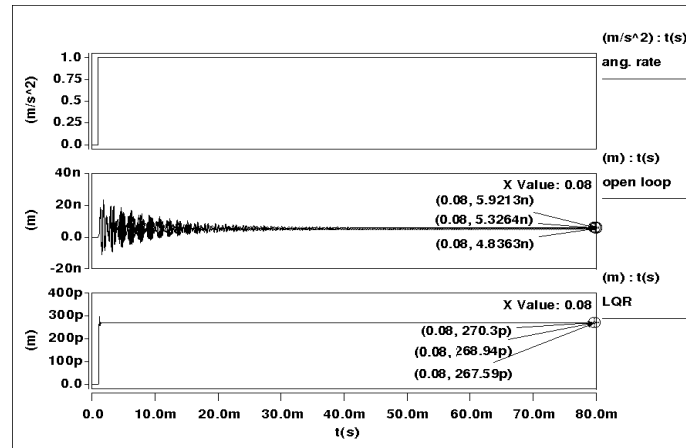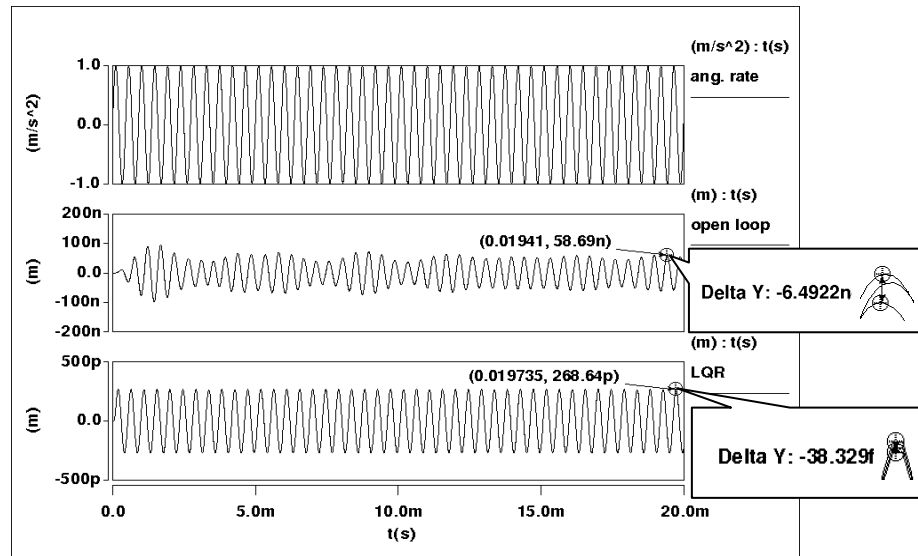

Figure 6.8. Sinusoidal response (2.2 kHz) of the non-resonant gyroscope under k_{2x} variations: (top trace) angular rate input, (middle trace) open-loop response, and (bottom trace) closed-loop response.

The results reported in this session are summarized in Fig. 6.9. Under the step input, the open-loop non-resonant gyroscope is very vulnerable to the spring constant variations. The scale factor is over 18% under ±10% k_{2x} variations. With the

89

compensator gain K of 3.54×10^9, the LQR control system has a scale factor error of 1.0%. Under the sinusoidal input which simulates the gyroscope in operation, although the open-loop non-resonant gyroscope is less vulnerable compared to the functional resonant gyroscopes, the scale factor error is over 11.06% under ±10% k_{2x} variations. The LQR controlled system significantly reduces the scale factor error to 0.014% which is over two orders of magnitude less error than the open-loop non-resonant gyroscope.
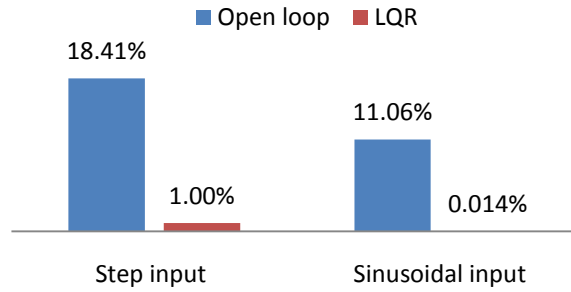
Figure 6.9. Summary of scale factor change under ±10% k_{2x} variations.

6.4 Discussions and conclusions

Although the non-resonant gyroscope has proved to be less vulnerable than the resonant gyroscope, under ±10% perturbation ratio, our results show that an open-loop non-resonant gyroscope has an 18.41% and 11.06% scale factor error under the step input and the sinusoidal input (at the designed operational frequency), respectively. A sense-mode control loop is designed for a non-resonant gyroscope to further improve the robustness to the parameter variations. The compensator is designed via LQR technique. The closed-loop system has a settling time of 0.5 ms which is shorter than the system without control loop (40 ms). Under ±10% perturbation ratio, the scale factor uniformity error is improved to 1.00% and 0.014% under the step input and the sinusoidal input,

90

respectively. Under the sinusoidal input which simulates the non-resonant gyroscope in operation, the compensator presents two orders of magnitude less error than the open-loop non-resonant gyroscope design.

CHAPTER SEVEN

CONCLUSIONS AND FUTURE WORK

7.1 Conclusions

In this thesis, we address two factors which contribute to the challenges in MEMS gyroscopes: 1) the coupling domains of MEMS gyroscopes hamper the fast development of new designs and 2) micro-fabrication imperfections lead to significant uncertainties of device scale factor in mass production. The specific achievements are presented as follows.

This research realizes the fast simulation using system-level models in CoventorWare. MEMS devices are traditionally simulated using FEM and boundary element method (BEM). However, these methods have tradeoffs in time, skill level restrictions, and limitations on the scope of the design problem. The system-level models significantly shorten the simulation time with relative high accuracy. The effect of viscous damping can be considered; the resulting model of the gyroscope is more accurate. Our simulation results of the damping coefficients are verified by the analytical slide-film and the squeeze-film models.

This research also investigates device performance uncertainties due to the fabrication imperfections and environmental variations. We demonstrate an integrated simulation workflow that incorporates the modeling of fabrication process, design optimization and packaging analysis. Design sensitivity analysis suggests that the device performance is highly sensitive to the suspension beam width. A 0.2 μm variation in a beam width can lead to a drive mode resonant frequency shift of over 1000 Hz. With a

small sample Monte Carlo analysis, the yield of gyroscope mass production is estimated to be 75%, provided that the acceptable range for the drive mode frequency is within ±3% deviation from its nominal value. Package analysis is also performed to model the packaged sensor undergoing extreme operation temperature. The results show that the maximum temperature-induced frequency shift in the MEMS device is less than 100 Hz in a temperature range from -40 °C to 120 °C. The gyroscope 3D model is generated based on mask layout and fabrication process restrictions. Typical MEMS simulation mainly focuses on device performance without taking fabrication process and packaging integratibility into account. This practice often leads to an inefficient product development cycle and increases the cost. The multi-level simulation reported in this research has proven to be an efficient way to speed up the design process and improve the device performance, and can be used effectively to optimize the gyroscope system.

This research also designs the robust compensators by LQR technique to improve the scale factor accuracy of the MEMS gyroscopes. The closed-loop MEMS device performance is simulated using system-level models in CoventorWare. Compared to an 18% open-loop error, the closed-loop scale factor error of the resonant gyroscope is reduced to 0.7% under ±10% parameter perturbations. For the open-loop non-resonant gyroscope, under ±10% parameter perturbations, the scale factor error is 18.41% under the step input and 11.06% under the sinusoidal input (within the robust frequency range). With the robust compensator, the closed-loop scale factor error is reduced to 1% and 0.014%, respectively, showing promising Inertial grade performance. Simulation shows that the closed-loop gyroscope is able to achieve high linearity, wide dynamic range, and

93

high robustness. LQR is an effective design to control MEMS gyroscopes and provides high robustness against fabrication imperfections.

7.2 Future work

In the current work, we have conducted multi-level simulation for the open-loop gyroscopes and implemented the robust compensator in CoventorWare. However, the multi-level simulation is not conducted for the closed-loop gyroscopes. For the future work, the simulation such as sensitivity analysis, Monte Carlo analysis, and package analysis, can be performed for the closed-loop gyroscopes. The sensitivity analysis is an efficient method to study the effect of design parameters on the resonant frequency. Monte Carlo analysis uses statistical distributions to randomly vary design parameters during successive simulations. The results reveal the influence of each design parameter on performance in mass production. The package analysis investigates the effect of temperature variations on the performance. The multi-level simulation should reveal the closed-loop performance under different excitation functions.

Moreover, the previous research has addressed that the major issues limiting the use of the gyroscopes to Tactical grade applications are the scale factor accuracy and the temperature drift. In this research, we investigate the scale factor accuracy under parameter variations. The scale factor accuracy under the package deformation and the temperature drift over the whole temperature range, however, are not discussed. These two issues remain to be studied in the next step. In [28], the scale factor accuracy and the temperature drift are calculated through the frequency shift due to the temperature variations.   The results can be easily obtained via the package analysis.

Additionally, in this research, the drive-mode control is assumed to be already setup and the amplitude of the drive-mode motion is well sustained (AGC control scheme [48]). In the future work, the drive-mode loop control should be developed. The design objective for the drive-mode loop is to track a non-decaying sinusoidal input at the drive-mode frequency and reject a non-decaying disturbance such as a step, ramp, or sinusoidal input at other frequencies. One possible solution is using the error-space approach, which allows to determine user-desired the reference input (the sinusoidal input at the drive-mode frequency) [30]. The resulting compensator is able to achieve the zero steady-state under the given excitation, even in the presence of perturbations of the original system parameters.

BIBLIOGRAPHY

[1]   Acar, C. and Shkel, A., 2008. MEMS vibratory gyroscopes, Springer.

[2]   Emerging MEMS technologies & markets - 2010 report. [Online]. Available: http://www.sensorsportal.com/DOWNLOADS/Emerging_MEMS.pdf, Accessed: May, 2010.

[3]   Elwenspoek, E. and Wiegerink, R., 2001. Mechanical Microsensors, Springer.

[4]   MEMS accelerometer, gyroscope and IMU market 2008-2013. [Online]. Available: http://www.yole.fr/pagesAn/products/pdf/Yole_World_Inertial_Sensors_Accelerometer_ Gyroscope_IMU_market_Flyer.pdf, Accessed: May, 2010.

[5]   Yazdi, N. et al., 1998. "Micromachined inertial sensors", Proceedings of the IEEE, 86(8), 1640–1659.

[6]   Maenaka, K. and Shiozawa, T., 1994. "A study of silicon angular rate sensors using anisotropic etching technology", Sensors and Actuators A: Physical, 43(1-3), 72–77.

[7]   Maenaka, K. et al., 1996. "Analysis of a highly sensitive silicon gyroscope with cantilever beam as vibrating mass", Sensors and Actuators A: Physical, 54(1-3), 568–573.

[8]   Putty, M. and Najafi, K., 1994. "A micromachined vibrating ring gyroscope", International Conference on Solid-State Sensor and Actuator Workshop, Hilton Head Island, SC, 213–220.

[9]   Bernstein, J. et al., 1993. "A micromachined comb-drive tuning fork rate gyroscope", Digest IEEE/ASME Microelectromechanical Systems, (MEMS) Workshop, Ft. Lauderdale, FL, 143–148.

[10] Hashimoto, M. et al., 1995. "Silicon resonant angular rate sensor using electromagnetic excitation and capacitive detection", Journal of Micromechanics and Microengineering, 5(3), 219–225.

[11] Greiff, P. et al., 1991. "Silicon monolithic micromechanical gyroscope", Technical Digest 6th International Conference Solid-State Sensors and Actuators (Transducers'91), San Francisco, CA, 966–968.

[12] Lutz, M. et al., 1997. "A precision yaw rate sensor in silicon micromachining", 9th international Conference on Solid-State Sensors and Actuators (Transducers'97), Chicago, IL, 847–850.

[13] Lynch, D., 1984. "Hemispherical resonator gyro", in Ragan, R. (Ed.) "Inertial technology for the future", IEEE Transactions on Aerospace and Electronic Systems, AES-20(4), 414–444.

[14] A Micromachined Quartz Angular Rate Sensor for Automotive and Advanced Inertial Applications. [Online]. Available: http://www.sensorsmag.com/sensors/position-presence-proximity/a-micromachined-quartz-angular-rate-sensor-automotive-and-ad-1071, Accessed: May, 2010.

[15] Nonomura, Y. et al., 2004. "Quartz rate gyro sensor for automotive control", Sensors and Actuators A: Physical, 110(1-3), 136–141.

[16] Safety and Performance Enhancement: the Bosch Electronic Stability Control (Esp) [Online]. Available: http://www.sae.org/technical/papers/2004-21-0060, Accessed: May, 2010.

[17] Funk, K. et al., 1999. "A surface micromachined silicon gyroscope using a thick polysilicon layer", 12th IEEE International Conference on Micro Electro Mechanical Systems (MEMS'99), Orlando, FL, 57–60.

[18] Neul, R. et al., 2005. "Micromachined gyros for automotive applications," 4th IEEE Conference Sensors, Irvine, CA, 527–530.

[19] Neul, R. et al., 2007. "Micromachined angular rate sensors for automotive applications," IEEE Sensors Journal,7(2), 302–309.

[20] Li, X. et al., 2006. "A microgyroscope with piezoresistance for both high-performance Coriolis-effect detection and seesaw-like vibration control", Journal of Microelectromechanical Systems, 15(6), 1698–1707.

[21] Günthner, S. et al., 2006. "Compensation of parasitic effects for a silicon tuning fork gyroscope", IEEE Sensors Journal, 6(3), 598–604.

[22] Acar, C. and Shkel, A. M., 2001. "Four degrees-of-freedom micromachined gyroscopes", Journal of Modeling and Simulation of Microsystems, 2(1), 71–82.

[23] Acar, C. and Shkel, A. M., 2003. "Non-resonant micromachined gyroscopes with structural mode-decoupling", IEEE Sensors Journal, 3(4), 487–506.

[24] Acar, C. and Shkel, A. M., 2003. "Structural design and experimental characterization of torsional micromachined gyroscopes with non-resonant drive mode", Journal of Micromechanics and Microengineering, 14, 15–25.

[25] Acar, C. and Shkel, A. M., 2005. "An approach for increasing drive mode bandwidth of MEMS vibratory gyroscopes", Journal of Microelectromechanical systems, 14(3), 520–528.

[26] Acar, C. et al., 2006. "Inherently robust micromachined gyroscopes with 2-DOF sense mode oscillator", Journal of Microelectromechanical Systems, 15(2), 380–387.

[27] Trusov, A. et al., 2008. "New Architectural Design of a Temperature Robust MEMS Gyroscope with Improved Gain-Bandwidth Characteristics," Solid-State Sensors, Actuators, and Microsystems Workshop 2008, Hilton Head Island, SC, 14–17.

[28] Trusov, A. et al., 2009. "Performance characterization of a new temperature-robust gain-bandwidth improved MEMS gyroscope operated in air", Sensors and Actuators A: Physical, 155(1), 16–22.

[29] Trusov, A., 2009. "Investigation of factors affecting bias stability and scale factor drifts in Coriolis vibratory MEMS gyroscopes", Ph.D dissertation, University of California, Irvine.

[30] Franklin, G. F. et al., 2002. Feedback control of dynamic systems, 4th ed., Prentice Hall.

[31] Jeon, H. and Grunwald, D., 2005. "Design of servo control systems with quadratic optimal control and observed-state feedback control for MEMS-based storage device", Microsystem Technologies, 11(8-10), 1005–1012.

[32] Gyimesi, M. et al., 2004. "Finite-element simulation of micro-electromechanical systems (MEMS) by strongly coupled electromechanical transducers", IEEE Transactions on Magnetics, 40(2), 557–560.

[33] Zhang, C. et al., 2006. "3D MEMS design method via Solidworks", Proceedings of 1st IEEE International Conference on Nano/Micro Engineering and Molecular Systems, 747–751.

[34] CoventorWare ACHITECT Reference, 2008.

[35] Park, S. and Horowitz, R., 2003. "Adaptive control for the conventional mode of operation of MEMS gyroscopes". Journal of Microelectromechanical Systems, 12(1), 101–108.

[36] Park, S. et al., 2008. "Dynamics and control of a MEMS angle measuring gyroscope". Sensors and Actuators A: Physical, 144(1), 56–63.

[37] Song, J. W. et al., 2002. "Feedback controller design for an in-plane gimbaled micro gyroscope using H∞ and state weighted model reduction techniques". Proceedings of International Conference on Computer Applications in Shipbuilding, Muju Resort, Korea, 228–233.

[38] Sung, W. T. et al., 2004. "H∞ controller design of MEMS gyroscope and its performance test". Proceedings of Positions, Location, and Navigation Symposium, Monterey, CA, 63–69.

[39] Fei, J. and Batur, C., 2009. "A novel adaptive sliding mode control with application to MEMS gyroscope". ISA Transactions, 48(1), 73–78.

[40] Chen, Y. et al., 2005. "A control and signal processing integrated circuit for the JPL-Boeing micromachined gyroscopes". IEEE Transactions on Control Systems Technology, 13(2), 286–300.

[41] Grayver, E. and M'Closkey, R. T., 2001. "Automatic gain control ASIC for MEMS gyro applications". American Control Conference, Arlington, VA, 1219–1222.

[42] Sung, W. T. et al., 2005. "PD controller design of micro gyroscope and its performance test". Journal of Korean Society for Aeronautical and Space Sciences, 33(3), 47–56.

[43] Sung, W. T. et al., 2008. "Controller design a MEMS gyro-accelerometer with a single proof mass". International Journal of Control, Automation, and Systems, 6(6), 873–883.

[44] Kraft, M., 1997. "Closed loop digital accelerometer employing over sampling conversion". PhD thesis, Coventry University, UK.

[45] Oboe, R. et al., 2005. "Control of a Z-axis MEMS vibrational gyroscope". IEEE/ASME Transactions on Mechatronics, 10(4), 364–370.

[46] Alper, S. E. and Akin, T., 2005. "A single-crystal silicon symmetrical and decoupled MEMS gyroscope on an insulating substrate". Journal of Microelectromechanical Systems, 14(4), 707–717.

[47] Alper, S. E. et al., 2008. "A compact angular rate sensor system using a fully decoupled silicon-on-glass MEMS gyroscope". Journal of Microelectromechanical Systems, 17(6), 1418–1429.

[48] Sung, W. T. et al., 2007. "Design and performance test of a MEMS vibratory gyroscope with a novel AGC force rebalance control". Journal of Micromechanics and Microengineering, 17(10), 1939–1948.

[49] Cui, W. et al., 2009. "Design optimization for a non-resonant gyroscope". Proceedings of ASME International Mechanical Engineering Congress and Exposition, Lake Buena Vista, FL, IMECE2009-10812.

[50] Liu, C., 2006. Foundations of MEMS, Prentice Hall.

[51] Acar, C., 2004. "Robust micromachined vibratory gyroscopes", Ph.D dissertation, University of California, Irvine.

[52] Blech, J., 1983. "On isothermal squeeze films", Journal of Lubrication Technology, 105, 615–620.

[53] Sumali, H., 2007. "Squeeze-film damping in the free molecular regime: model validation and measurement on a MEMS", Journal of Micromechanics and Microengineering, 17(11), 2231–2240.

[54] Chen, X. et al., 2009. "Process modeling and device-package simulation for optimization of MEMS gyroscopes", Computer-Aided Design and Applications, 6(3), 375–386.

MATLAB CODE

A. Compensator design for a non-resonant gyroscope

```
clear all;
clc
m2=7.67e-7;   %proof mass m₂
c2=2e-7;    %damping coefficient c₂ₓ
k2=144;       %spring constant k₂ₓ

m3=7.29e-8;   %proof mass m₃
c3=3e-5;    %damping coefficient c₃ₓ
k3=13.6;       %spring constant k₃ₓ

numG_X2=[m2*m3 m2*c3 m2*k3];     %numerator of the transfer
function (X2)
denG_X2=[m2*m3 c2*m3+m2*c3 k2*m3+k3*m3+c2*c3+m2*k3
k2*c3+k3*c3+c2*k3 k2*k3];        %dominator of the transfer
function (X2)
sysG_X2=tf(numG_X2,denG_X2);

numG_X3=k3*m2;  %numerator of the transfer function (X3)
denG_X3=denG_X2;     %dominator of the transfer function (X3)
sysG_X3=tf(numG_X3,denG_X3);

sysG=tf(numG_X3,denG_X3);
%%%%%Open loop performance%%%%%
figure(11)
step(sysG)
figure(12)
rlocus(sysG)
figure(13)
bode(sysG)

%%%%%Implement SRL Method%%%%%%%
numGG1_X3=numG_X3;
numGG2_X3=numGG1_X3;

denGG1_X3=denG_X3;
denGG2_X3=denGG1_X3;

numGG=conv(numG_X3,numG_X3);
```

```
for n=1:2
    denGG2_X3(2*n)=-denGG1_X3(2*n);
end
denGG=conv(denGG1_X3,denGG2_X3);
sysGG=tf(numGG,denGG);    %sysGG=G(s)*G(-s)

p1=5.5e19;  %parameters to choose poles of the controller
p2=6.25e26; %parameters to choose poles of the estimator

pc=poles(numGG,denGG,p1)  %call 'poles.m' and select stable
roots of sysGG based on p1
pe=poles(numGG,denGG,p2)  %call 'poles.m' and select stable
roots of sysGG based on p2


F=[0 1 0 0 ;
    -(k2+k3)/m2,-c2/m2,k3/m2,0;
     0 0 0 1;
     k3/m3 0 -k3/m3 -c3/m3];    %system matrix
G=[0 1 0 0]';                   %input matrix
H=[0 0 1 0];                    %output matrix
J=0;                           %transmission matrix

K=acker(F,G,pc)   %determine control gain K which is a row
vector
L=acker(F',H',pe) %estimator(filter)gain L. L is a row
vector
LL=L';            %LL is a column vector

%%%%%Determine the Compensator%%%%%%%
FF=F-G*K-LL*H;
[Cnum,Cden]=ss2tf(FF,LL,K,0)   %LQR compensator
sysC=tf(Cnum,Cden) %sysC is the transfer function of the
compensator

sysGC=sysG*sysC;  % plant * compensator


%%%%%Closed-loop system in the standard form%%%%%%%
Ac=zeros(8,8);
Ac(1:4,1:4)=F;
Ac(1:4,5:8)=-G*K;
Ac(5:8,1:4)=LL*H;
Ac(5:8,5:8)=F-G*K-LL*H;
Bc=zeros(8,1);
```

```
Nbar=2.68e-10;   %scale factor Nbar

Bc(2)=1/Nbar;    %inverse of the scale factor
Cc=zeros(1,8);
Cc(1:4)=H;

%%%%%Simulation Results%%%%%%%
figure(1)
step(Ac,Bc,Cc,0)
figure(2)
rlocus(Ac,Bc,Cc,0)
```

B. M-file of function Poles.m

```
% This function will pick out stable roots from the
symmetric root locus.

%Inputs:
%    numGG      numerator of the symmetric root locus
%    denGG      denominator of the symmetric root locus
%    p          weighting factor

%Ouputs:
%    pp         stable roots of the symmetric root locus


function pp=poles(numGG,denGG,p)
numGG=numGG*p;
len1=length(numGG);
len2=length(denGG);
if len1>len2
    temp=numGG(len1-len2+1:len1);
    temp=temp+denGG;
    equ=cat(2,numGG(1:len1-len2),temp);
elseif len1<len2
    temp=denGG(len2-len1+1:len2);
    temp=temp+numGG;
    equ=cat(2,denGG(1:len2-len1),temp);
else
    equ=numGG+denGG;
end
rts=roots(equ); %all the roots in both left and right
planes

len=length(rts);
j=1;
for i=1:len
    if real(rts(i))<0
        pp(j)=rts(i);% poles in the left plane (stable
roots)
        j=j+1;
    end
end
```

C. Symmetric root locus plot with the design criteria of the resonant gyro (Figure 4.3)

```
clear all
clc
m=1.3e-9;
c=0.4e-6;
k=30.48;
numG=[m];
denG=[m,c,k];
sysG=tf(numG,denG)

numGG=[1]
denGG=conv([m,-c,k],[m,c,k]);
sysGG=tf(numGG,denGG)

A=rlocus(sysGG,'r'); %collect data points of the root locus

B=real(A)/2/pi;      %x coordinates of the data. Covnert to
Herz
C=imag(A)/2/pi;      %y coordinates of the data. Covnert to
Herz

figure(1)
for i=1:4
plot(B(i,1),C(i,1),'*')
plot(B(i,:),C(i,:),'b','linewidth',[2])
hold on
end
title('Root Locus')
ylabel('Imaginary Axis (Hz)')
xlabel('Real Axis (Hz)')


x1=-30e3:10:30e3;        %draw a circle and indicate a
bandwideth of 30k
y1=sqrt(30e3^2-x1.^2);
y2=-sqrt(30e3^2-x1.^2);
plot(x1,y1,'k--',x1,y2,'k--')
hold on

xx1=-5.69e5/2/pi       %draw two markers,indicate the scale


factor error of 1%
```

```
yy1=5.89e5/2/pi;
yy2=-5.89e5/2/pi;
plot(xx1,yy1,'kdiamond',xx1,yy2,'kdiamond','markersize',[10
])
hold on

x4=-1e6:1e4:1e6;
xlim([-1.2e5,1.2e5])
ylim([-1.2e5,1.2e5])
x5=-5e6:5e3:5e6;
len=length(x5)
plot(0,x5,'k:',x5,0,'k:')  %draw X and Y axises
hold off
```

D. The open-loop and closed-loop bode of the resonant gyro (Figure 4.4)

```
clear all; clc
Ms=1.3e-009;
Bs=0.4e-6;
Ks=30.68;
numG=[Ms];
denG=[Ms Bs Ks];
sysG=tf(numG,denG);

F=[0 1;
    -Ks/Ms -Bs/Ms];
G=[0 1]';
H=[1 0];
J=0

numC=5e11*[2e-6 1]; %designed compensator
denC=[2e-7 1];

sysC=tf(numC,denC);

figure(1)
sysGC=sysG*sysC;  %open-loop transfer function

[A,B,Rad]=bode(sysGC); %A is the magnitude, B is phase, Rad
is the frequency (rad/s)

len=length(A);
Hz=Rad/2/pi;
for i=1:len
    mag(i)=A(:,:,i); %A is mag, B is phase
    phase(i)=B(:,:,i);
end

subplot(2,2,1)
loglog(Hz,mag,'linewidth',[2])
xlim([1e4 1e7])
set(gca,'xtick',[1e4 1e5 1e6 1e7])
set(gca,'ytick',[1e-5 0.003162277 1 316.2277 1e5])
set(gca,'yticklabel',[-100 -50 0 50 100])
ylabel('Magnitude (dB)')
set(gca,'xticklabel',[])
grid on


title('Open-loop Bode')
```

```
subplot(2,2,3)
semilogx(Hz,phase,'linewidth',[2])
xlim([1e4 1e7])
set(gca,'xtick',[1e4 1e5 1e6 1e7])
set(gca,'ytick',[-180 -135 -90 -45 0 45])
ylim([-180 45])
ylabel('Phase (deg)')
xlabel('Frequency (Hz)')
grid on

sysGCH=sysG/(1+sysG*sysC); %closed-loop transfer function
[A2,B2,Rad2]=bode(sysGCH); %A2 is mag, B2 is phase
len2=length(A2);
Hz2=Rad2/2/pi;
for i=1:len2
    mag2(i)=A2(:,:,i);
    phase2(i)=B2(:,:,i);
end
mag2=log10(mag2)*20;  % convert to dB
subplot(2,2,2)
semilogx(Hz2,mag2,'linewidth',[2])
xlim([1e4 1e6])
set(gca,'xticklabel',[])
grid on
title('Closed-loop Bode')
BW=(max(mag2)-3)*ones(len2);

hold on
plot(Hz2,BW)

subplot(2,2,4)
semilogx(Hz2,phase2,'linewidth',[2])
xlim([1e4 1e6])
ylim([-180 0])
set(gca,'ytick',[-180 -135 -90 -45 0])
set(gca,'xtick',[1e4 1e5 1e6])
xlabel('Frequency (Hz)')
grid on
```